Ground state search, hysteretic behaviour, and reversal mechanism of skyrmionic textures in confined helimagnetic nanostructures

Marijan Beg,[1, *] Rebecca Carey,[1] Weiwei Wang,[1] David Cortés-Ortuño,[1] Mark Vousden,[1] Marc-Antonio Bisotti,[1] Maximilian Albert,[1] Dmitri Chernyshenko,[1] Ondrej Hovorka,[1] Robert L. Stamps,[2] and Hans Fangohr[1, †]

[1]*Faculty of Engineering and the Environment, University of Southampton, Southampton SO17 1BJ, United Kingdom*
[2]*SUPA School of Physics and Astronomy, University of Glasgow, Glasgow G12 8QQ, United Kingdom*

Magnetic skyrmions have the potential to provide solutions for low-power, high-density data storage and processing. One of the major challenges in developing skyrmion-based devices is the skyrmions' magnetic stability in confined helimagnetic nanostructures. Through a systematic study of equilibrium states, using a full three-dimensional micromagnetic model including demagnetisation effects, we demonstrate that skyrmionic textures are the lowest energy states in helimagnetic thin film nanostructures at zero external magnetic field and in absence of magnetocrystalline anisotropy. We also report the regions of metastability for non-ground state equilibrium configurations. We show that bistable skyrmionic textures undergo hysteretic behaviour between two energetically equivalent skyrmionic states with different core orientation, even in absence of both magnetocrystalline and demagnetisation-based shape anisotropies, suggesting the existence of Dzyaloshinskii-Moriya-based shape anisotropy. Finally, we show that the skyrmionic texture core reversal dynamics is facilitated by the Bloch point occurrence and propagation.

An ever increasing need for data storage creates great challenges for the development of high-capacity storage devices that are cheap, fast, reliable, and robust. Nowadays, hard disk drive technology uses magnetic grains pointing up or down to encode binary data (0 or 1) in so-called perpendicular recording media. Practical limitations are well understood and dubbed the "magnetic recording trilemma" [1]. It defines a trade-off between three conflicting requirements: signal-to-noise ratio, thermal stability of the stored data, and the ability to imprint information. Because of these fundamental constraints, further progress requires radically different approaches.

Recent research demonstrated that topologically stable magnetic skyrmions have the potential for the development of future data storage and information processing devices. For instance, a skyrmion lattice formed in a monoatomic Fe layer grown on a Ir(111) surface [2] revealed skyrmions with diameters as small as a few atom spacings. In addition, it has been demonstrated that skyrmions can be easily manipulated using spin-polarised currents of the $10^6 \, \text{A m}^{-2}$ order [3, 4] which is a factor 10^5 to 10^6 smaller than the current densities required in conventional magneto-electronics. These unique skyrmion properties point to an opportunity for the realisation of ambitious novel high-density, power-efficient storage [5, 6] and logic [7] devices.

Skyrmionic textures emerge as a consequence of chiral interactions, also called the Dzyaloshinskii-Moriya Interactions (DMI), that appear when there is no inversion symmetry in the magnetic system structure. The lack of inversion symmetry can be either due to a noncentrosymmetric crystal lattice structure [8, 9] in so-called helimagnetic materials, or at interfaces between different materials that inherently lack inversion symmetry [10, 11]. According to this, the Dzyaloshinskii-Moriya

interaction can be classified either as bulk or interfacial, respectively. Skyrmions, after being predicted [12–14], were later experimentally observed in magnetic systems with both bulk [15–19] and interfacial [2, 20] types of DMI.

So far, a major challenge obstructing the development of skyrmion-based devices has been their thermal and magnetic stability [21]. Only recently, skyrmions were observed at the room temperature in magnetic systems with bulk [22] and interfacial [23–25] DMI. However, the magnetic stability of skyrmions in absence of external magnetic field was reported only for magnetic systems with interfacial DMI in one-atom layer thin films [2, 26], where the skyrmion state is stabilised in the presence of magnetocrystalline anisotropy.

The focus of this work is on the zero-field stability of skyrmionic textures in confined geometries of bulk DMI materials. Zero-field stability is a crucial requirement for the development of skyrmion-based devices: devices that require external magnetic fields to be stabilised are volatile, harder to engineer and consume more energy. We address the following questions that are relevant for the skyrmion-based data storage and processing nanotechnology. Can skyrmionic textures be the ground state (i.e. have the lowest energy) in helimagnetic materials at zero external magnetic field, and if they can, what is the mechanism responsible for this stability? Do the demagnetisation energy and magnetisation variation along the out-of-film direction [27] have important contribution to the stability of skyrmionic textures? Is the magnetocrystalline anisotropy an essential stabilisation mechanism? Are there any other equilibrium states that emerge in confined helimagnetic nanostructures? How robust are skyrmionic textures against varying geometry? Do skyrmionic textures undergo hysteretic behaviour in the presence of an external magnetic field (crucial for

data imprint), and if they do, what is the skyrmionic texture reversal mechanism?

To resolve these unknowns, we use a full three-dimensional simulation model that makes no assumption about translational invariance of magnetisation in the out-of-film direction and takes full account of the demagnetisation energy. We demonstrate, using this full model, that DMI-induced skyrmionic textures in confined thin film helimagnetic nanostructures are the lowest energy states in the absence of both the stabilising external magnetic field and the magnetocrystalline anisotropy and are able to adapt their size to hosting nanostructures, providing the robustness for their practical use. We demonstrate that both the demagnetisation energy and the magnetisation variation in the out-of-film direction play an important role for the stability of skyrmionic textures. In addition, we report the parameter space regions where other magnetisation configurations are in equilibrium. Moreover, we demonstrate that these zero-field stable skyrmionic textures undergo hysteretic behaviour when their core orientation is changed using an external magnetic field, which is crucial for data imprint. The hysteretic behaviour remains present even in the absence of all relevant magnetic anisotropies (magnetocrystalline and demagnetisation-based shape anisotropies), suggesting the existence of a novel Dzyaloshinskii-Moriya-based shape anisotropy. We conclude the study by showing that the skyrmionic texture core orientation reversal is facilitated by the Bloch point occurrence and propagation, where the Bloch point may propagate in either of the two possible directions. This work is based on the specific cubic helimagnetic material, FeGe with 70 nm helical period, in order to encourage the experimental verification of our predictions. Other materials could allow either to reduce the helical period [15, 19] and therefore the hosting nanostructure size or increase the operating temperature [22].

Some stability properties of DMI-induced isolated skyrmions in two-dimensional confined systems have been studied analytically [28–30] and using simulations [26, 31]. However, in all these studies, either magnetocrystalline anisotropy or an external magnetic field (or both) are crucial for the stabilisation of skyrmionic textures. In addition, an alternative approach to the similar problem, in absence of chiral interactions, where skyrmionic textures can be stabilised at zero external magnetic field and at room temperature using a strong perpendicular anisotropy, has been studied analytically [32], experimentally [33, 34], as well as using simulations [35]. Our new results, and in particular the zero-field skyrmionic ground state in isotropic helimagnetic materials, can only be obtained by allowing the chiral modulation of magnetisation direction along the film normal, which has recently been shown to radically change the skyrmion energetics [27].

RESULTS

Equilibrium states. In order to identify the lowest energy magnetisation state in confined helimagnetic nanostructures, firstly, all equilibrium magnetisation states (local energy minima) must be identified, and secondly, their energies compared. In this section, we focus on the first step – identifying the equilibrium magnetisation states. We compute them by solving a full three-dimensional model using a finite element based micromagnetic simulator. In particular, we simulate a thin film helimagnetic FeGe disk nanostructure with thickness $t = 10$ nm and diameter d, as shown in Fig. 1 inset. The finite element mesh discretisation is such that the maximum spacing between two neighbouring mesh nodes is below 3 nm. The material parameters are $M_s = 384$ kA m^{-1}, $A = 8.78$ pJ m^{-1}, and $D = 1.58$ mJ m^{-2}. We apply a uniform external magnetic field perpendicular to the thin film sample, i.e. in the positive z-direction. The Methods section contains the details about the model, FeGe material parameters estimation, as well as the simulator software.

In this section, we determine what magnetisation configurations emerge as the equilibrium states at different d–H parameter space points. In order to do that, we systematically explore the parameter space by varying the disk sample diameter d from 40 nm to 180 nm and the external magnetic field $\mu_0 H$ from 0 T to 1.2 T in steps of $\Delta d = 4$ nm and $\mu_0 \Delta H = 20$ mT, respectively. At every point in the parameter space, we minimise the energy for a set of different initial magnetisation configurations: (i) five different skyrmionic configurations, (ii) three helical-like configurations with different helical period, (iii) the uniform out-of-plane configuration, and (iv) three random magnetisation configurations. We use the random magnetisation configurations in order to capture other equilibrium states not obtained by relaxing the well-defined initial magnetisation configurations. The details on how we define and generate initial magnetisation configurations are provided in the Supplementary Section S1.

The equilibrium states to which different initial magnetisation configurations relax in the energy minimisation process (at every d–H parameter space point) we present in the Supplementary Section S2 as a set of "relaxation diagrams". We summarise these relaxation diagrams and determine the phase space regions where different magnetisation states are in equilibrium, and show them in Fig. 1. Among the eight computed equilibrium states, three are radially symmetric and we label them as iSk, Sk, and T, whereas the other states, marked as H2, H3, H4, 2Sk, and 3Sk, are not. Subsequently, we discuss the meaning of the chosen labels.

Now, we focus on the analysis of radially symmetric skyrmionic equilibrium states, supported by computing
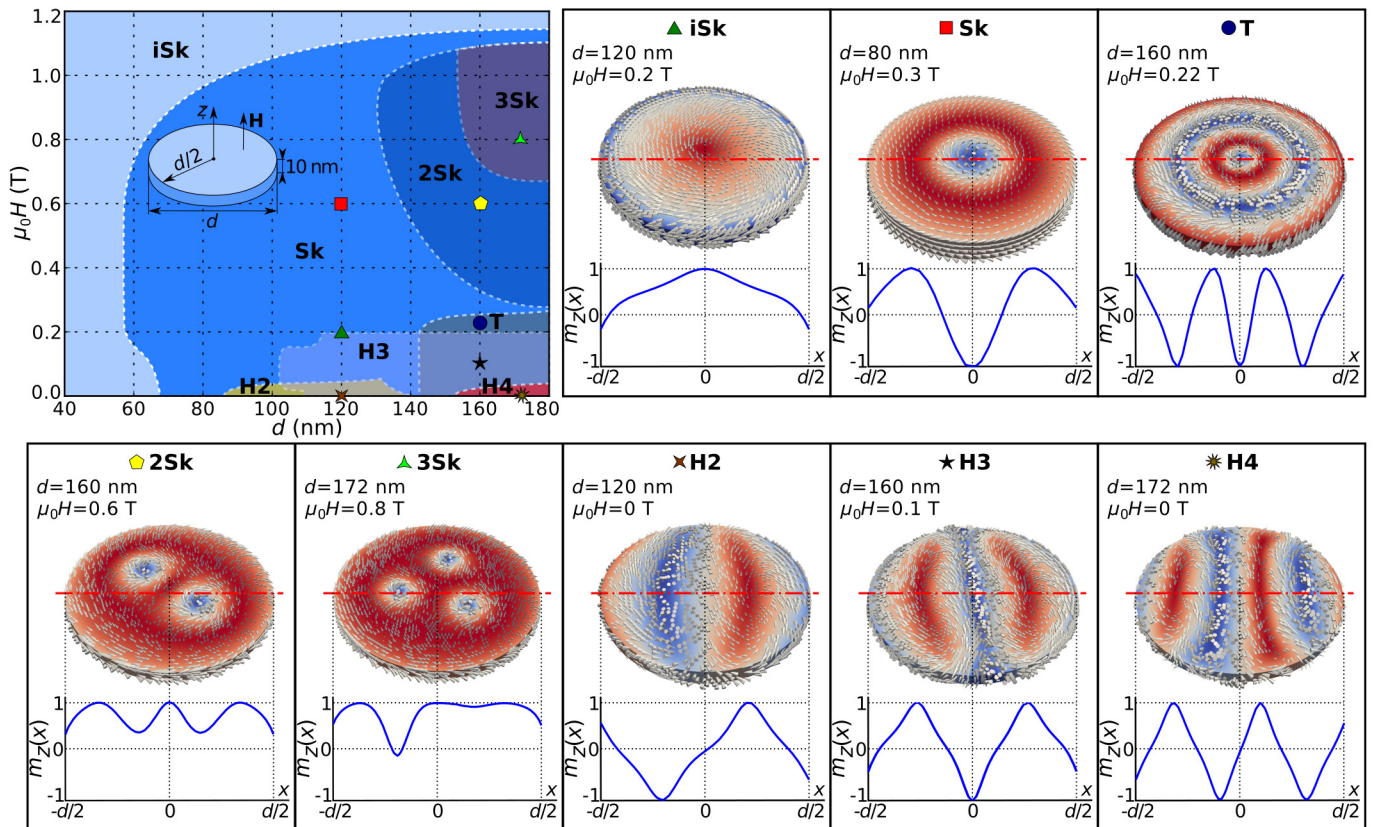
FIG. 1. **The metastability phase diagram and magnetisation configurations of all identified equilibrium states.**
The phase diagram with regions where different states are in equilibrium together with magnetisation configurations and out-of-plane magnetisation component $m_z(x)$ along the horizontal symmetry line corresponding to different regions in the phase diagram.

the skyrmion number S and scalar value S_a as defined in the Methods section. In the first configuration, marked in Fig. 1 as iSk, the out-of-plane magnetisation component $m_z(x)$ profile along the horizontal symmetry line does not cover the entire $[-1, 1]$ range, as would be the case for a skyrmion configuration (where the magnetisation vector field **m** needs to cover the whole sphere). Accordingly, the scalar value S_a (Eq. (6) in the Methods section, and plotted in Supplementary Fig. 2 (b) for a range of configurations), is smaller than 1. For these reasons we refer to this skyrmionic equilibrium state as the incomplete Skyrmion (iSk) state. A similar magnetisation configuration has been predicted and observed in other works for the case of two-dimensional systems in the presence of magnetocrystalline anisotropy where it is called either the quasi-ferromagnetic [26, 28] or edged vortex state [29, 31]. Because the iSk equilibrium state clearly differs from the ferromagnetic configuration and using the word vortex implies the topological charge of $1/2$, we prefer calling this state the incomplete skyrmion state. The incomplete Skyrmion (iSk) state emerges as an equilibrium state in the entire simulated d–H parameter space range. In the second equilibrium state, marked

as Sk in Fig. 1, $m_z(x)$ covers the entire $[-1, 1]$ range, the magnetisation covers the sphere at least once and, consequently, the skyrmion configuration is present in the simulated sample. Although the skyrmion number value (Eq. (5) in the Methods section) for this solution is $|S| < 1$ due to the additional magnetisation tilting at the disk boundary [28], which makes it indistinguishable from the previously described iSk equilibrium state, the scalar value is $1 < S_a < 2$. This state is referred to as the isolated Skyrmion or just Skyrmion (Sk), in two-dimensional systems [26, 28], and we use the same name subsequently in this work. We find that the Sk state is not in equilibrium for sample diameters smaller than 56 nm and external magnetic field values larger than approximately 1.14 T. Finally, the equilibrium magnetisation state marked as T in Fig. 1 covers the sphere at least twice. In other works, this state together with all other predicted higher-order solutions (not observed in this work) are called the "target states" [30], and we use the same Target (T) state name. The analytic model, used for generating initial states, also predicts the existence of higher-order target states (Supplementary Fig. 2 (c)). The T magnetisation configuration emerges as an equi-

librium state for samples with diameter $d \geq 144\,\text{nm}$ and field values $\mu_0 H \leq 0.24\,\text{T}$.

The equilibrium states lacking radial symmetry can be classified into two groups: helical-like (marked as H2, H3, and H4) and multiple skyrmion (marked as 2Sk and 3Sk) states. The difference between the three helical-like states is in their helical period. More precisely, in the studied range of disk sample diameter values, either 2, 3, or 4 helical half-periods, including the additional magnetisation tilting at the disk sample edge due to the specific boundary conditions [28], fit in the sample diameter. Consequently, we refer to these states, that occur as an equilibrium state for samples larger than 88 nm and field values lower than 0.2 T, as H2, H3, and H4 . The other two radially non-symmetric equilibrium states are the multiple skyrmion configurations with 2 or 3 skyrmions present in the sample and we call these equilibrium states 2Sk and 3Sk, respectively. These configurations emerge as equilibrium states for samples with $d \geq 132\,\text{nm}$ and external magnetic field values between $0.28\,\text{T} \leq \mu_0 H \leq 1.06\,\text{T}$.

Ground state. After we identified all observed equilibrium states in confined helimagnetic nanostructures, in this section we focus on finding the equilibrium state with the lowest energy at all d–H parameter space points. For every parameter space point (d, H), after we compute and compare the energies of all found equilibrium states, we determine the lowest energy state, and refer to it, in this context, as the ground state. For the identified ground state, we compute the scalar value S_a and use it for plotting a d–H phase diagram shown in Fig. 2 (a). Discontinuous changes in the scalar value S_a define the boundaries between regions where different magnetisation configurations are the ground state. In the studied phase space, two different ground states emerge in the confined helimagnetic FeGe thin film disk samples: one with $S_a < 1$ and the other with $1 < S_a < 2$. The previous discussion of the S_a value suggests that these two regions correspond to the incomplete Skyrmion (iSk) and the isolated Skyrmion (Sk) states. We confirm this by visually inspecting two identified ground states, taken from the two phase space points (marked with circle and triangle symbols) in different regions, and show them in Fig. 2 (b) together with their out-of-plane magnetisation component $m_z(x)$ along the horizontal symmetry line.

A key result of this study is that both incomplete Skyrmion (iSk) and isolated Skyrmion (Sk) are the ground states at zero external magnetic field for different disk sample diameters. More precisely, iSk is the ground state for samples with diameter $d < 140\,\text{nm}$ and Sk is the ground state for $d \geq 140\,\text{nm}$. The Sk changes to the iSk ground state for large values of external magnetic field.

The phase diagram in Fig. 2 shows the phase space regions where iSk and Sk are the ground states, which means that all other previously identified equilibrium
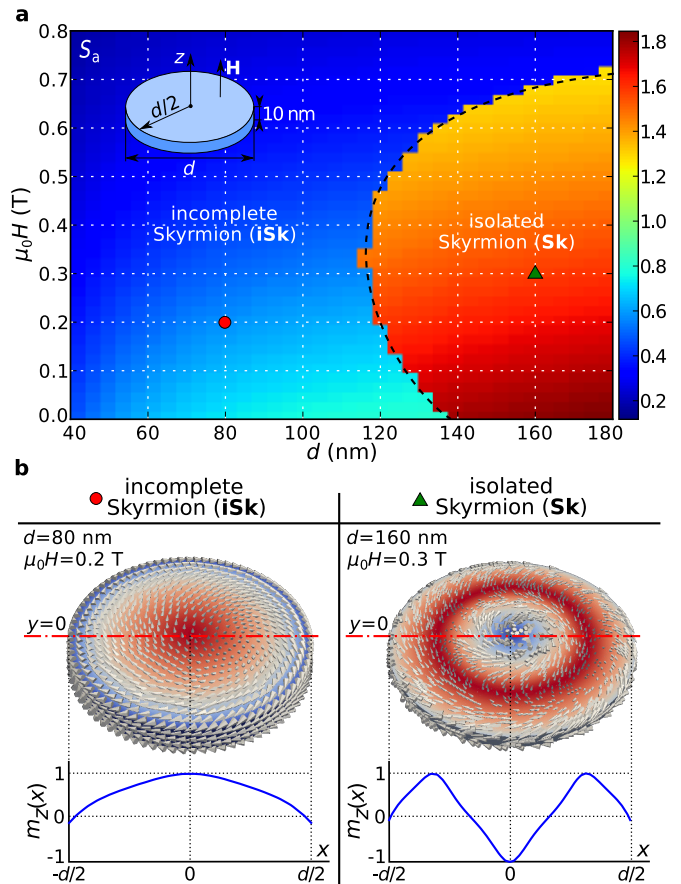

FIG. 2. **Thin film disk ground state phase diagram and corresponding magnetisation states.** (**a**) The scalar value S_a for the thin film disk sample with thickness $t = 10\,\text{nm}$ as a function of disk diameter d and external out-of-plane magnetic field **H** (as shown in an inset). (**b**) Two identified ground states: incomplete Skyrmion (iSk) and isolated Skyrmion (Sk) magnetisation configurations at single phase diagram points together with their out-of-plane magnetisation component $m_z(x)$ profiles along the horizontal symmetry line.

states are metastable. Now, we focus on computing the energies of metastable states relative to the identified ground state. Firstly, we compute the energy density E/V for all equilibrium states, where E is the total energy of the system and V is the disk sample volume, and then subtract the ground state energy density corresponding to that phase space point. We show the computed energy density differences $\Delta E/V$ when the disk sample diameter is changed in steps of $\Delta d = 2\,\text{nm}$ at zero external magnetic field in Fig. 3 (a). Similarly, the case when the disk sample diameter is $d = 160\,\text{nm}$ and the external magnetic field is changed in steps of $\mu_0 \Delta H = 20\,\text{mT}$ is shown in Fig. 3 (b). The magnetisation configurations are the equilibrium states in the d or H values range where the line is shown and collapse otherwise.
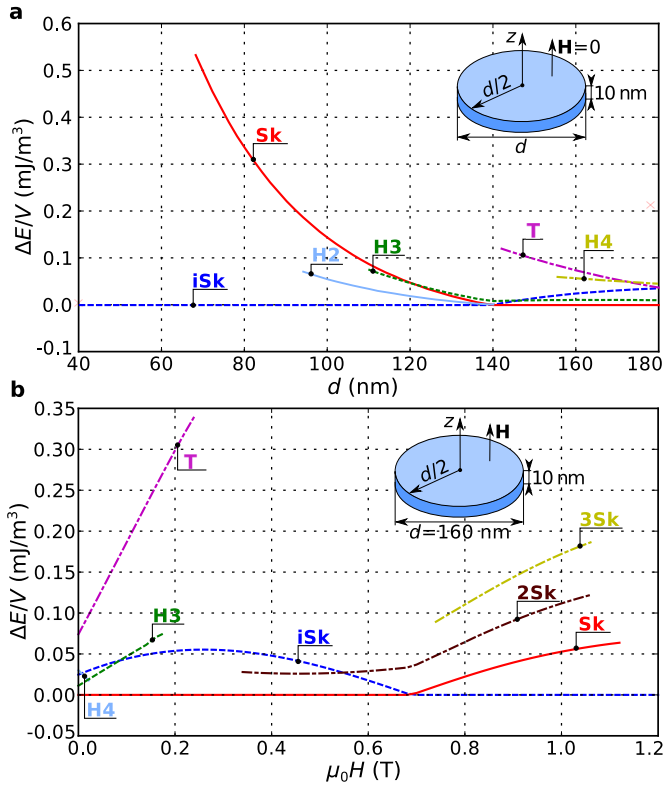
FIG. 3. **The energy density difference between identified equilibrium states and the corresponding ground state.** Energy density differences $\Delta E/V$ at (**a**) zero field for different sample diameters d and for (**b**) sample diameter $d = 160$ nm and different external magnetic field values. Configurations are in equilibrium where the line is shown and collapse for other diameter or external magnetic field values.

FIG. 4. **The $m_z(x)$ profiles and skyrmionic texture sizes s for different sizes of hosting nanostructures at zero external magnetic field.** (**a**) Profiles of the out-of-plane magnetisation component $m_z(x)$ along the horizontal symmetry line for different thin film disk sample diameters with thickness $t = 10$ nm at zero external magnetic field $\mu_0 H = 0$ T. The curves for $d \leq 120$ nm represent incomplete skyrmion ($\circ$) states, and for $d \geq 140$ nm represent isolated skyrmion ($\times$) states. (**b**) The skyrmionic texture size $s = 2\pi/k$ (that can be interpreted as the length along which the full magnetisation rotation occurs) as a function of the hosting nanostructure size, obtained by fitting $m_z(x) = \pm\cos(kx)$ to the simulated profile. (**c**) The ratio of skyrmionic texture size to disk sample diameter (s/d) as a function of hosting nanostructure size d.

For the practical use of ground state skyrmionic textures in helimagnetic nanostructures, their robustness is of great significance due to the unavoidable variations in the patterning process. Because of that, in Fig. 4 (a) we plot the out-of-plane magnetisation component $m_z(x)$ along the horizontal symmetry line for the iSk and the Sk ground state at zero external magnetic field for six different diameters d of the hosting disk nanostructure: three iSk profiles for $d \leq 120$ nm, and three Sk profiles for $d \geq 140$ nm. The profiles show that the two skyrmionic ground states have the opposite core orientations. In the case of the Sk states, the magnetisation at the core is antiparallel and at the outskirt parallel to the external magnetic field. This reduces the Zeeman energy $E_z = -\mu_0 \int \mathbf{H} \cdot \mathbf{M} \, d^3\mathbf{r}$ because the majority of the magnetisation in the isolated skyrmion outskirts points in the same direction as the external magnetic field $\mathbf{H}$. Once the disk diameter is sufficiently small that less than a complete spin rotation fits into the sample, this orientation is not energetically favourable anymore and the iSk state emerges. In this iSk state, the core magnetisation points in the same direction as the external magnetic
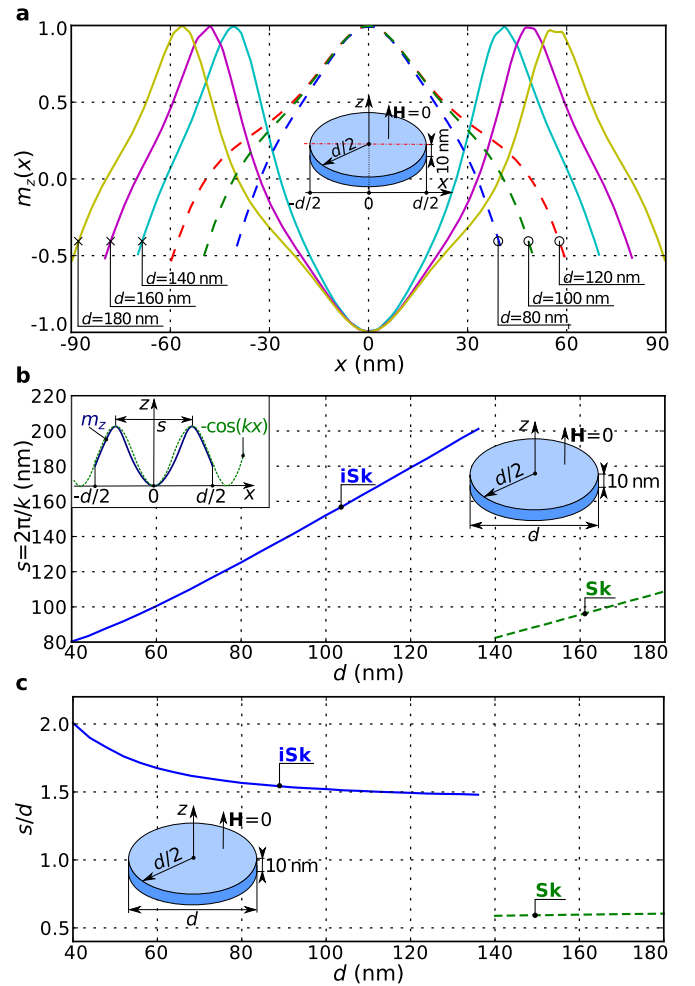
field in order to minimise the Zeeman energy. We compute and plot the skyrmionic texture size $s = 2\pi/k$ as a function of the disk sample diameter d in Fig. 4 (b). We obtain the size s, that can be interpreted as the length along which the full magnetisation rotation occurs, by fitting k in the $f(x) = \pm\cos(kx)$ function to the simulated iSk and Sk $m_z(x)$ profiles. In Fig. 4 (c), we show how the ratio of skyrmionic texture size to disk sample diameter (s/d) depends on the hosting nanostructure

size. Although this ratio is constant ($s/d \approx 0.6$) for the Sk state, in the iSk case, it is larger for smaller samples and decreases to $s/d \approx 1.5$ in larger nanostructures. In agreement with related findings for two-dimensional disk samples [29] we find that both iSk and Sk are able to change their size s in order to accommodate the size of hosting nanostructure, which provides robustness for the technological use.

The emergence of skyrmionic texture ground state in helimagnetic nanostructures at zero external magnetic field and in absence of magnetocrystalline anisotropy is unexpected [21]. Now, we discuss the possible mechanisms, apart from the geometrical confinement, responsible for this stability, in particular (i) the demagnetisation energy contribution, and (ii) the magnetisation variation along the out-of-film direction which can radically change the skyrmion energetics in infinitely large helimagnetic thin films [27]. We repeat the simulations using the same method and model as above but ignoring the demagnetisation energy contribution (i.e. setting the demagnetisation energy density w_d in Eq. (1) artificially to zero). We then carry out the calculations (i) on a three-dimensional (3d) mesh (i.e. with spatial resolution in z-direction) and (ii) on a two-dimensional (2d) mesh (i.e. with no spatial resolution in z-direction, and thus not allowing a variation of the magnetisation along the z-direction). The disk sample diameter d is changed between 40 nm and 180 nm in steps of $\Delta d = 5$ nm and the external magnetic field $\mu_0 H$ is changed systematically between 0 T and 0.5 T in steps of $\mu_0 \Delta H = 25$ mT. The two resulting phase diagrams are shown in Fig. 5, where subplots (a) and (c) show S_a as a function of d and H. Because the scalar value S_a does not provide enough contrast to determine the boundaries of the new Helical (H) ground state region, the skyrmion number S is plotted for the relevant phase diagram areas and shown in Fig. 5 (b) and Fig. 5 (d).

We demonstrate the importance of including demagnetisation effects into the model by comparing Fig. 5 (a) (without demagnetisation energy) and Fig. 2 (a) (with demagnetisation energy). In the absence of the demagnetisation energy, the isolated Skyrmion (Sk) configuration is not found as the ground state at zero applied field; instead, Helical (H) configurations have lower energies. At the same time, the external magnetic field at which the skyrmion configuration ground state disappears is reduced from about 0.7 T to about 0.44 T.

By comparing Fig. 5 (a) computed on a 3d mesh and Fig. 5 (c) computed on a 2d mesh, we can see the importance of spatial resolution in the out-of-plane direction of the thin film, and how it contributes to the stabilisation of isolated Skyrmion (Sk) state. In the 2d model, the field range over which skyrmions can be observed as the ground state is further reduced to approximately [0.05 T, 0.28 T]. In the 3d mesh model the Sk configuration can reduce its energy by twisting the magnetisation

at the top of the disk relative to the bottom of the disk so that along the z-direction the magnetisation starts to exhibit (a part of) the helix that arises from the competition between symmetric exchange and DMI energy terms, similar to Ref. [27]. A similar twist provides no energetic advantage to the helix configuration, thus the Sk state region in Fig. 5 (a) is significantly larger than the Sk state region in Fig. 5 (c) where the 2d mesh does not allow any variation of the magnetisation along the z-direction and thus the partial helix cannot form.

While the isolated Skyrmion (Sk) configuration at zero field is a metastable state in the absence of demagnetisation energy, or in 2d models, it is not the ground state anymore as there are Helical (H) equilibrium configurations that have lower total energy. The demagnetisation energy appears to suppress these helical configurations which have a lower energy than the skyrmion. The variation of the magnetisation along the z-direction stabilises the skyrmion configuration substantially. These findings demonstrate the subtle nature of competition between symmetric exchange, DM and demagnetisation interactions, and show that ignoring the demagnetisation energy or approximating the thin film helimagnetic samples using two-dimensional models is not generally justified.

Hysteretic behaviour. The phase diagram in Fig. 2 (a) shows the regions in which incomplete Skyrmion (iSk) and isolated Skyrmion (Sk) configurations are the ground states. Intuitively, one can assume that for every sample diameter d at zero external magnetic field, there are two possible skyrmionic magnetisation configurations of equivalent energy: core pointing up or core pointing down, suggesting that these textures can be used for an information bit (0 or 1) encoding. We now investigate this hypothesis and study whether an external magnetic field can be used to switch the skyrmionic state orientation (crucial for data imprint) by simulating the hysteretic behaviour of ground state skyrmionic textures.

We obtain the hysteresis loops in the usual way by evolving the system to an equilibrium state after changing the external magnetic field, and then using the resulting state as the starting point for a new evolution. In this way, a magnetisation loop takes into account the history of the magnetisation configuration. The external magnetic field $\mu_0\mathbf{H}$ is applied in the positive z-direction and changed between -0.5 T and 0.5 T in steps of $\mu_0 \Delta H = 5$ mT. The hysteresis loops are represented as the dependence of the average out-of-plane magnetisation component $\langle m_z \rangle$ on the external magnetic field H. The hysteresis loop for a 10 nm thin film disk sample with $d = 80$ nm diameter in which the incomplete Skyrmion (iSk) is the ground state is shown in Fig. 6 (a) as a solid line. Similarly, a solid line in Fig. 6 (b) shows the corresponding hysteresis loop for a larger disk sample with
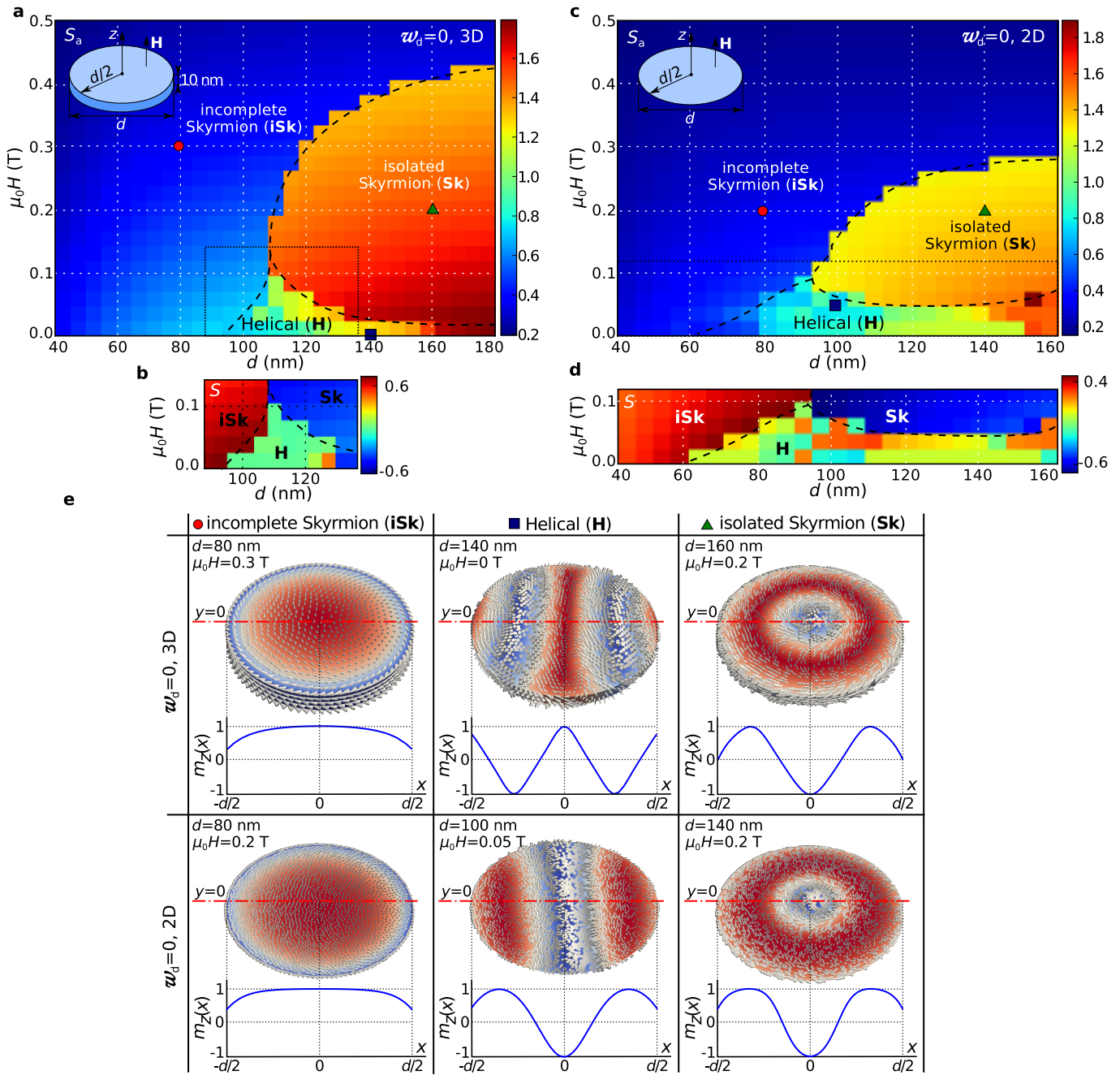
FIG. 5. **The ground state phase diagram in absence of demagnetisation energy contribution.** The scalar value S_a as a function of disk sample diameter d and external magnetic field H computed for the ground state at every phase space point in absence of demagnetisation energy contribution for (**a**) a 3d mesh and (**c**) for a 2d mesh. In order to better resolve the boundaries of the Helical (H) state region, the skyrmion number S is shown in (**b**) and (**d**). (**e**) The magnetisation configurations of three identified ground states as well as the out-of-plane magnetisation component $m_z(x)$ along the horizontal symmetry line.

$d = 150$ nm diameter in which the isolated Skyrmion (Sk) is the ground state. The hysteresis between two energetically equivalent skyrmionic magnetisation states with the opposite core orientation at zero external magnetic field, shown in Fig. 6 (c), is evident. Moreover, the system does not relax to any other equilibrium state at any point in the hysteresis loop, which demonstrates the bistability of skyrmionic textures in studied system. The area of the open loop in the hysteresis curve is a measure of the work needed to reverse the core orientation by overcoming the energy barrier separating the two skyrmionic states with opposite core orientation.
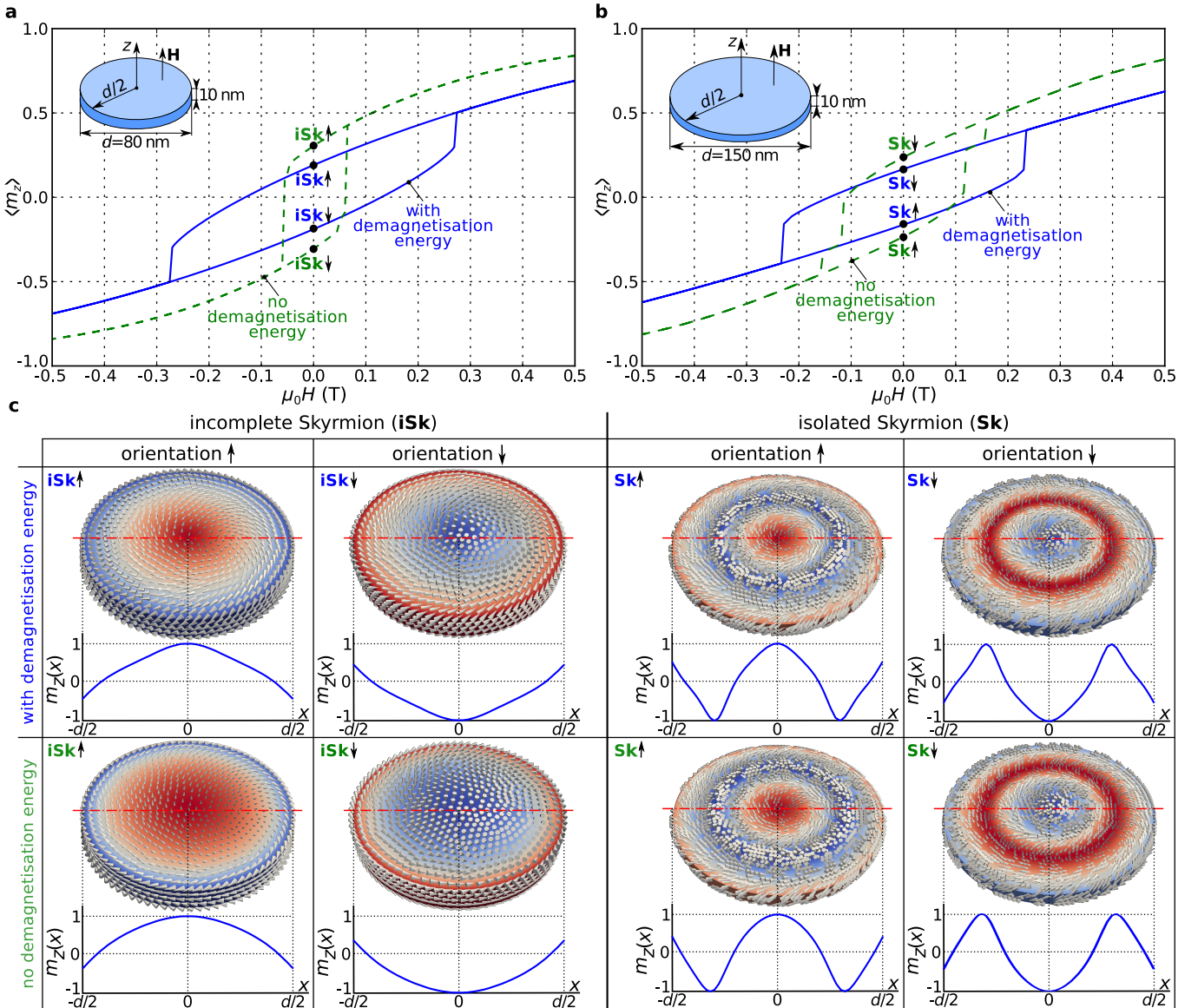
FIG. 6. **Hysteresis loops and obtained zero-field skyrmionic states with different orientations.** The average out-of-plane magnetisation component $\langle m_z \rangle$ hysteretic dependence on the external out-of-plane magnetic field H for 10 nm thin film disk samples for (**a**) incomplete Skyrmion (iSk) magnetisation configuration in $d = 80$ nm diameter sample and (**b**) isolated Skyrmion (Sk) magnetisation configuration in $d = 150$ nm diameter sample. (**c**) The magnetisation states and $m_z(x)$ profiles along the horizontal symmetry lines for positive and negative iSk and Sk core orientations from $H = 0$ in the hysteresis loop, both in presence and in absence of demagnetisation energy (demagnetisation-based shape anisotropy).

As throughout this work, it is assumed that the simulated helimagnetic material is isotropic, and thus, the magnetocrystalline anisotropy energy contribution is neglected. Due to that, one might expect that the obtained hysteresis loops are the consequence of demagnetisation-based shape anisotropy. To address this, we simulate hysteresis using the same method, but this time in absence of the demagnetisation energy contribution. More precisely, the minimalistic energy model contains only the symmetric exchange and Dzyaloshinskii-Moriya interactions together with

Zeeman coupling to an external magnetic field. We show the obtained hysteresis loops in Fig. 6 (a) and (b) as dashed lines. The hysteretic behaviour remains, although all energy terms that usually give rise to the hysteretic behaviour (magnetocrystalline anisotropy and demagnetisation energies) were neglected. This suggests the existence of a new magnetic anisotropy that we refer to as the Dzyaloshinskii-Moriya-based shape anisotropy.

Reversal mechanism. The hysteresis loops in Fig. 6 show that skyrmionic textures in confined thin film he-

limagnetic nanostructures undergo hysteretic behaviour and that an external magnetic field can be used to change their orientation from core pointing up to core pointing down and vice versa. In this section, we discuss the mechanism by which the skyrmionic texture core orientation reversal occurs. We simulate a 150 nm diameter thin film FeGe disk sample with $t = 10$ nm thickness. The maximum spacing between two neighbouring finite element mesh nodes is reduced to 1.5 nm in order to better resolve the magnetisation field. According to the hysteresis loop in Fig. 6 (b), the switching field H_s of the isolated skyrmion state in this geometry from core orientation down to core orientation up is $\mu_0 H_s \approx -235$ mT. Therefore, we first relax the system at -210 mT external magnetic field and then decrease it abruptly to -250 mT. We simulate the magnetisation dynamics for 1 ns, governed by a dissipative LLG equation [36] with Gilbert damping $\alpha = 0.3$ [26], and record it every $\Delta t = 0.5$ ps.

We now look at how certain magnetisation configuration parameters evolve during the reversal process. We show the time-dependent average magnetisation components $\langle m_x \rangle$, $\langle m_y \rangle$, and $\langle m_z \rangle$ in Fig. 7 (a), and on the same time axis, the skyrmion number S, scalar value S_a and total energy E in Fig. 7 (b). The initial magnetisation configuration at $t = 0$ ns is denoted as A and the final relaxed magnetisation at $t = 1$ ns as F. We show in Fig. 7 (c) the out-of-plane magnetisation field component m_z in the whole sample, in the xz cross section, as well as along the horizontal symmetry line. At approximately 662 ps the skyrmionic core reversal occurs and Fig. 7 (b) shows an abrupt change both in skyrmion number S and total energy E. We summarise the reversal process with the help of six snapshots shown in Fig. 7 (c). Firstly, in (A-B), the isolated skyrmion core shrinks. At some point the maximum m_z value lowers from 1 to approximately 0.1 (C). After that, the core reverses its direction (D) and an isolated skyrmion of different orientation is formed (E). From that time onwards, the core expands in order to accommodate the size of hosting nanostructure, until the final state (F) is reached. The whole reversal process is also provided in Supplementary Video 1.

In order to better understand the actual reversal of the skyrmionic texture core between $t_1 \approx 661$ ps and $t_2 \approx 663$ ps, we show additional snapshots of the magnetisation vector field and m_z colourmap in the xz cross section in Fig. 7 (d). The location marked by a circle in subplots L, M, and N identifies a Bloch Point (BP): a noncontinuous singularity in the magnetisation pattern where the magnetisation magnitude vanishes to zero [37, 38]. Because micromagnetic models assume constant magnetisation magnitude, the precise magnetisation configuration at the BP cannot be obtained using micromagnetic simulations [39]. However, it is known how to identify the signature of the BP in such situations: the magnetisation direction covers any sufficiently small closed surface surrounding the BP exactly once [40, 41].

We illustrate this property in Fig. 7 (e) using a vector plot together with m_x, m_y, and m_z colour plots that show the structure of a Bloch point. We conclude that the isolated skyrmion core reversal occurs via Bloch Point (BP) occurrence and propagation. Firstly, at $t \approx 661.5$ ps the BP enters the sample at the bottom boundary and propagates upwards until $t \approx 663$ ps when it leaves the sample at the top boundary. In the Supplementary Video 2 the isolated skyrmion core reversal dynamics is shown.

We note that the Bloch point moves upwards in Fig. 7 (d) but one may ask whether an opposite propagation direction can occur and how the Bloch point structure is going to change. We demonstrate that which of these two propagation directions will occur in the reversal process depends on the simulation parameters. The reversal mechanism simulation was repeated with increased Gilbert damping ($\alpha = 0.35$ instead of $\alpha = 0.3$) and the results showing the downwards propagation are shown in the Supplementary Section S3. We hypothesise that both reversal paths (Bloch point moving upwards or downwards) exhibit the same energy barriers and that the choice of path is a stochastic process. By analysing the results from Fig. 7 (d) and (e) and Supplementary Fig. 6, we also observe that the change in the BP propagation direction implies the change of the BP structure since the out-of-plane magnetisation component m_z field reverses in the vicinity of BP.

DISCUSSION

Through systematic micromagnetic study of equilibrium states in helimagnetic confined nanostructures, we identified the ground states and reported the (meta)stability regions of other equilibrium states. We demonstrated in Fig. 2 that skyrmionic textures in the form of incomplete Skyrmion (iSk) and isolated Skyrmion (Sk) configurations are the ground states in disk nanostructures, and that this occurs in a wide d–H parameter space range. We have carried out similar studies for a square geometry and obtain qualitatively similar results. Of particular importance is that iSk and Sk states are the ground states at zero external magnetic field which is in contrast to infinite thin film and bulk helimagnetic samples. We note that neither an external magnetic field is necessary nor magnetocrystalline anisotropy is required for this stability. We also note in Fig. 4 (c) that there is significant flexibility in the skyrmionic texture size which provides robustness for technology built on skyrmions, where fabrication of nanostructures and devices introduces unavoidable variation in geometries.

We have established that including the demagnetisation interaction is crucial for the system investigated here, i.e. in the absence of demagnetisation effects, there are other magnetisation configurations with energies lower than that of the incomplete and isolated
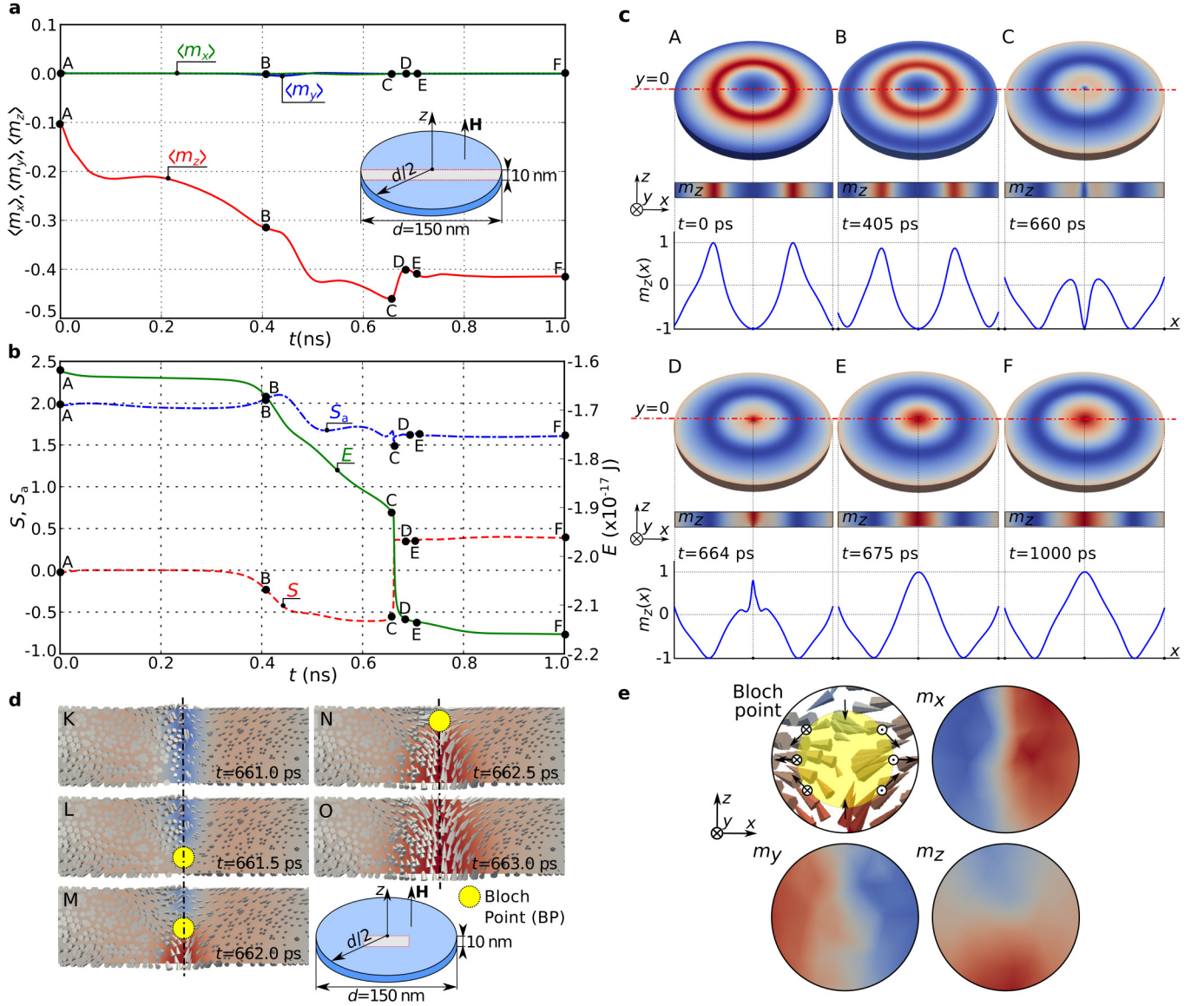
FIG. 7. **The isolated skyrmion orientation reversal in confined three-dimensional helimagnetic nanostructure.** (**a**) The spatially averaged magnetisation components $\langle m_x \rangle$, $\langle m_y \rangle$, and $\langle m_z \rangle$ and (**b**) skyrmion number S, scalar value S_a, and total energy E time evolutions in the reversal process over 1 ns. The simulated sample is a 10 nm thin film disk with 150 nm diameter. (**c**) The magnetisation states at different instances of time (points A to F) together with m_z colourmap in the xz cross section and $m_z(x)$ profiles along the horizontal symmetry line. (**d**) The m_z colourmap and magnetisation field in the central part of xz cross section as shown in an inset together with the position of Bloch point (BP). (**e**) The BP structure along with colourmaps of magnetisation components which shows that the magnetisation covers the closed surface (sphere surrounding the BP) exactly once.

skyrmion. We also note that the translational variance of the magnetisation from the lower side of the thin film (at $z = 0$ nm) to the top (at $z = 10$ nm) is essential for the physics reported here: if we use a two-dimensional micromagnetic simulation (i.e. assuming translational invariance of the magnetisation $\mathbf{m}$ in the out-of-plane direction), the isolated skyrmion configuration does not arise as the ground state. Our interpretation is that for skyrmion-like configurations the twist of $\mathbf{m}$ between top

and bottom layer allows the system's energy to reduce significantly while such a reduction is less beneficial for other configurations such as helices; inline with recent predictions in the case of infinite thin films [27]. Accordingly, we conclude that three-dimensional helimagnetic nanostructure models, where demagnetisation energy contribution is neglected, or the geometry approximated using a two-dimensional mesh, are not generally justified.

Because of the specific boundary conditions [28] and the importance of including the demagnetisation energy contribution, our predictions cannot be directly applied to other helimagnetic materials without repeating the stability study. For instance, although the size of skyrmionic textures in this study was based on cubic FeGe helimagnetic material with helical period $L_{\mathrm{D}} = 70\,\mathrm{nm}$, in order to encourage the experimental verification of our predictions, this study could be repeated for materials with smaller L_{D}. In such materials the skyrmionic core size is considerably reduced, which allows the reduction of hosting nanostructure size and is an essential requirement for advancing future information storage technologies. Similarly, the ordering temperature of simulated FeGe helimagnetic material, $T_{\mathrm{C}} = 278.7\,\mathrm{K}$ [42], is lower than the room temperature, which means that a device operating at the room temperature cannot be constructed using this material. Because of that, in Supplementary Section S4, we demonstrate that our predictions are still valid if the ordering temperature of simulated B20 helimagnetic material is artificially increased to $350\,\mathrm{K}$.

We demonstrate in Fig. 6 that skyrmionic textures in confined helimagnetic nanostructures exhibit hysteretic behaviour as a consequence of energy barriers between energetically equivalent stable configurations (skyrmionic texture core pointing up or down). In the absence of magnetocrystalline anisotropy and if the demagnetisation energy (demagnetisation-based shape anisotropy) is removed from the system's Hamiltonian, the hysteretic behaviour is still present, demonstrating the existence of a novel Dzyaloshinskii-Moriya-based shape anisotropy.

Finally, we show how the reversal of the isolated skyrmion core orientation is facilitated by the Bloch point occurrence and propagation, and demonstrate that the Bloch point can propagate in both directions along the out-of-plane z-direction.

All data obtained by micromagnetic simulations in this study and used to create figures both in the main text and in the Supplementary Information are included in Supplementary Data.

METHODS

Model. We use an energy model consistent with a non-centrosymmetric cubic B20 ($P2_13$ space group) crystal structure. This is appropriate for a range of isostructural compounds and pseudo-binary alloys in which skyrmionic textures have been experimentally observed [3, 4, 15–18, 43, 44]. The magnetic free energy of the system E contains several contributions and can be written in the form:

$$E = \int \left[w_{\mathrm{ex}} + w_{\mathrm{dmi}} + w_{\mathrm{z}} + w_{\mathrm{d}} + w_{\mathrm{a}} \right] \mathrm{d}^3 r. \qquad (1)$$

The first term is the symmetric exchange energy density $w_{\mathrm{ex}} = A \left[(\nabla m_x)^2 + (\nabla m_y)^2 + (\nabla m_z)^2 \right]$ with exchange stiffness material parameter A, where m_x, m_y, and m_z are the Cartesian components of the vector $\mathbf{m} = \mathbf{M}/M_{\mathrm{s}}$ that describes the magnetisation $\mathbf{M}$, with $M_{\mathrm{s}} = |\mathbf{M}|$ being the saturation magnetisation. The second term is the Dzyaloshinskii-Moriya Interaction (DMI) energy density $w_{\mathrm{dmi}} = D\mathbf{m} \cdot (\nabla \times \mathbf{m})$, obtained by constructing the allowed Lifshitz invariants for the crystallographic class T [12, 45], where D is the material parameter. The third term is the Zeeman energy density term $w_{\mathrm{z}} = -\mu_0 \mathbf{H} \cdot \mathbf{M}$ which defines the coupling of magnetisation to an external magnetic field $\mathbf{H}$. The w_{d} term represents the demagnetisation (magnetostatic) energy density. The last term w_{a} is the magnetocrystalline anisotropy energy density, and because the simulated material is assumed to be isotropic, we neglect it throughout this work. Neglecting this term also allows us to determine whether the magnetocrystalline anisotropy is a crucial mechanism allowing the stability of skyrmionic textures in confined helimagnetic nanostructures.

The Landau-Lifshitz-Gilbert (LLG) equation [36]:

$$\frac{\partial \mathbf{m}}{\partial t} = \gamma^* \mathbf{m} \times \mathbf{H}_{\mathrm{eff}} + \alpha \mathbf{m} \times \frac{\partial \mathbf{m}}{\partial t}, \qquad (2)$$

governs the magnetisation dynamics, where $\gamma^* = \gamma(1+\alpha^2)$, with $\gamma < 0$ and α being the gyromagnetic ratio and Gilbert damping, respectively. We compute the effective magnetic field using $\mathbf{H}_{\mathrm{eff}} = -(\delta w/\delta \mathbf{m})/(\mu_0 M_{\mathrm{s}})$, where w is the total energy density functional. With this model, we solve for magnetic configurations $\mathbf{m}$ using the condition of minimum torque arrived by integrating a set of dissipative, time-dependent equations. We validated the boundary conditions by a series of simulations reproducing the results in Ref. [26, 28].

Simulator. We developed a micromagnetic simulation software, inspired by the Nmag simulation tool [46, 47]. Unlike Nmag, we use the FEniCS project [48] instead of the Nsim multi-physics library [46] for the finite element low-level operations. In addition, we use IPython [49, 50] and Matplotlib [51, 52] extensively in this work.

Material parameters. We estimate the material parameters in our simulations to represent the cubic B20 FeGe helimagnet with four Fe and four Ge atoms per unit cell [53] and crystal lattice constant $a = 4.7\,\text{Å}$ [54]. The local magnetic moments of iron and germanium atoms are $1.16\mu_{\mathrm{B}}$ and $-0.086\mu_{\mathrm{B}}$ [55], respectively, where μ_{B} is the Bohr magneton constant. Accordingly, we estimate the saturation magnetisation as $M_{\mathrm{s}} = 4N(1.16 - 0.086)\mu_{\mathrm{B}} = 384\,\mathrm{kA\,m^{-1}}$, with $N = a^{-3}$ being the number of lattice unit cells in a cubic metre. The spin-wave stiffness is $D_{\mathrm{sw}} = a^2 T_{\mathrm{C}}$ [56], where the FeGe ordering temperature is $T_{\mathrm{C}} = 278.7\,\mathrm{K}$ [42]. Consequently, the exchange stiffness parameter value

is $A = D_{sw}M_s/(2g\mu_B) = 8.78\,\mathrm{pJ\,m^{-1}}$ [57], where $g \approx 2$ is the Landé g-factor. The estimated DMI material parameter D from the long-range FeGe helical period $L_D = 70\,\mathrm{nm}$ [42], using $L_D = 4\pi A/|D|$ [43], is $|D| = 1.58\,\mathrm{mJ\,m^{-2}}$.

Skyrmion number S and injective scalar value S_a. In order to support the discussion of skyrmionic textures, the topological skyrmion number [2]

$$S^{2D} = \frac{1}{4\pi} \int \mathbf{m} \cdot \left(\frac{\partial \mathbf{m}}{\partial x} \times \frac{\partial \mathbf{m}}{\partial y} \right) \, \mathrm{d}^2 r, \qquad (3)$$

can be computed for two-dimensional samples hosting the magnetisation configuration. However, for confined systems, the skyrmion number S^{2D} is not quantised into integers [26, 31], and therefore, a more suitable name for S^{2D} may be the "scalar spin chirality" (and consequently the expression under an integral would be called the "spin chirality density"), but we will follow the existing literature [26, 31] and refer to S^{2D} as the skyrmion number. We show its dependence on different skyrmionic textures that can be observed in confined helimagnetic nanostructures in Supplementary Fig. 2 (b), demonstrating that the skyrmion number in confined geometries is not an injective function since it does not preserve distinctness (one-to-one mapping between skyrmionic textures and skyrmion number value S^{2D}). Therefore, for two-dimensional samples, we define a different scalar value

$$S_a^{2D} = \frac{1}{4\pi} \int \left| \mathbf{m} \cdot \left(\frac{\partial \mathbf{m}}{\partial x} \times \frac{\partial \mathbf{m}}{\partial y} \right) \right| \, \mathrm{d}^2 r, \qquad (4)$$

and show its dependence on different skyrmionic textures in Supplementary Fig. 2 (b). This scalar value is injective and provides necessary distinctness between S_a^{2D} values for different skyrmionic states. In terms of the terminology discussion above regarding S^{2D}, the entity S_a^{2D} describes the "scalar absolute spin chirality". We also emphasise that although the skyrmion number S^{2D} has a clear mathematical [58] and physical [59] interpretation, we define the artificial injective scalar value S_a only to support the classification and discussion of different skyrmionic textures observed in this work.

Skyrmion number S^{2D} and artificially defined scalar value S_a^{2D}, given by Eq. (3) and Eq. (4), respectively, are valid only for the two-dimensional samples hosting the magnetisation configuration. However, in this work, we also study three-dimensional samples and, because of that, we now define a new set of expressions taking into account the third dimension. The skyrmion number in three-dimensional samples S^{3D} we compute using

$$S^{3D} = \frac{1}{8\pi} \int \mathbf{m} \cdot \left(\frac{\partial \mathbf{m}}{\partial x} \times \frac{\partial \mathbf{m}}{\partial y} \right) \, \mathrm{d}^3 r, \qquad (5)$$

as suggested by Lee et al. [60], which results in a value proportional to the anomalous Hall conductivity. Similar to the two-dimensional case, we also define the artificial injective scalar value S_a^{3D} for three-dimensional samples as

$$S_a^{3D} = \frac{1}{8\pi} \int \left| \mathbf{m} \cdot \left(\frac{\partial \mathbf{m}}{\partial x} \times \frac{\partial \mathbf{m}}{\partial y} \right) \right| \, \mathrm{d}^3 r. \qquad (6)$$

In order to allow the S_a^{3D} value to fall within the two-dimensional skyrmionic textures classification scheme, we normalise the computed S_a^{3D} value by a constant ($t/2$, where t is the sample thickness).

For simplicity, in this work, we refer to both two-dimensional and three-dimensional skyrmion number and scalar value expressions as S and S_a because it is always clear what expression has been used according to the dimensionality of the sample.

REFERENCES

* mb4e10@soton.ac.uk
† h.fangohr@soton.ac.uk

[1] Richter, H. J. The transition from longitudinal to perpendicular recording. *J. Phys. D. Appl. Phys.* **40**, R149–R177 (2007).

[2] Heinze, S. *et al.* Spontaneous atomic-scale magnetic skyrmion lattice in two dimensions. *Nat. Phys.* **7**, 713–718 (2011).

[3] Jonietz, F. *et al.* Spin transfer torques in MnSi at ultralow current densities. *Science* **330**, 1648–1651 (2010).

[4] Yu, X. Z. *et al.* Skyrmion flow near room temperature in an ultralow current density. *Nat. Commun.* **3**, 988 (2012).

[5] Kiselev, N. S., Bogdanov, A. N., Schäfer, R. & Rößler, U. K. Chiral skyrmions in thin magnetic films: new objects for magnetic storage technologies? *J. Phys. D. Appl. Phys.* **44**, 392001 (2011).

[6] Fert, A., Cros, V. & Sampaio, J. Skyrmions on the track. *Nat. Nanotechnol.* **8**, 152–156 (2013).

[7] Zhang, X., Ezawa, M. & Zhou, Y. Magnetic skyrmion logic gates: conversion, duplication and merging of skyrmions. *Sci. Rep.* **5**, 9400 (2015).

[8] Dzyaloshinsky, I. A thermodynamic theory of weak ferromagnetism of antiferromagnetics. *J. Phys. Chem. Solids* **4**, 241-255 (1958).

[9] Moriya, T. Anisotropic superexchange interaction and weak ferromagnetism. *Phys. Rev.* **120**, 91–98 (1960).

[10] Fert, A. & Levy, P. M. Role of anisotropic exchange interactions in determining the properties of spin-glasses. *Phys. Rev. Lett.* **44**, 1538–1541 (1980).

[11] Crépieux, A. & Lacroix, C. DzyaloshinskyMoriya interactions induced by symmetry breaking at a surface. *J. Magn. Magn. Mater.* **182**, 341–349 (1998).

[12] Bogdanov, A. N. & Yablonskii, D. A. Thermodynamically stable "vortices" in magnetically ordered crystals. The mixed state of magnets. *Sov. Phys. JETP* **68**, 101–103 (1989).

[13] Bogdanov, A. & Hubert, A. Stability of vortex-like structures in uniaxial ferromagnets. *J. Magn. Magn. Mater.* **195**, 182–192 (1999).

[14] Rößler, U. K., Bogdanov, A. N. & Pfleiderer, C. Spontaneous skyrmion ground states in magnetic metals. *Nature* **442**, 797–801 (2006).

[15] Mühlbauer, S. *et al.* Skyrmion lattice in a chiral magnet. *Science* **323**, 915–919 (2009).

[16] Yu, X. Z. *et al.* Near room-temperature formation of a skyrmion crystal in thin-films of the helimagnet FeGe. *Nat. Mater.* **10**, 106–109 (2011).

[17] Yu, X. Z. *et al.* Real-space observation of a two-dimensional skyrmion crystal. *Nature* **465**, 901–904 (2010).

[18] Seki, S., Yu, X. Z., Ishiwata, S. & Tokura, Y. Observation of skyrmions in a multiferroic material. *Science* **336**, 198–201 (2012).

[19] Kanazawa, N. *et al.* Possible skyrmion-lattice ground state in the B20 chiral-lattice magnet MnGe as seen via small-angle neutron scattering. *Phys. Rev. B* **86**, 134425 (2012).

[20] Romming, N. *et al.* Writing and deleting single magnetic skyrmions. *Science* **341**, 636–639 (2013).

[21] Editorial. Skyrmionics in sight. *Nat. Nanotechnol.* **8**, 883 (2013).

[22] Tokunaga, Y. *et al.* A new class of chiral materials hosting magnetic skyrmions beyond room temperature. *Nat. Commun.* **6**, 7638 (2015).

[23] Woo, S. *et al.* Observation of room temperature m agnetic skyrmion s and their current-driven dynamics in ultrathin Co films. *arXiv* 1502.07376, URL `http://arxiv.org/abs/1502.07376` (2015). Date of access: 08/09/2015.

[24] Moreau-Luchaire, C. *et al.* Skyrmions at room temperature : From magnetic thin films to magnetic multilayers. *arXiv* 1502.07853, URL `http://arxiv.org/abs/1502.07853` (2015). Date of access: 08/09/2015.

[25] Jiang, W. *et al.* Blowing magnetic skyrmion bubbles. *Science* **349**, 283–286 (2015).

[26] Sampaio, J., Cros, V., Rohart, S., Thiaville, A. & Fert, A. Nucleation, stability and current-induced motion of isolated magnetic skyrmions in nanostructures. *Nat. Nanotechnol.* **8**, 839–844 (2013).

[27] Rybakov, F. N., Borisov, A. B. & Bogdanov, A. N. Three-dimensional skyrmion states in thin films of cubic helimagnets. *Phys. Rev. B* **87**, 094424 (2013).

[28] Rohart, S. & Thiaville, A. Skyrmion confinement in ultrathin film nanostructures in the presence of Dzyaloshinskii-Moriya interaction. *Phys. Rev. B* **88**, 184422 (2013).

[29] Du, H., Ning, W., Tian, M. & Zhang, Y. Magnetic vortex with skyrmionic core in a thin nanodisk of chiral magnets. *EPL* **101**, 37001 (2013).

[30] Leonov, A. O., Rößler, U. K. & Mostovoy, M. Target-skyrmions and skyrmion clusters in nanowires of chiral magnets. *EPJ Web Conf.* **75**, 05002 (2014).

[31] Du, H., Ning, W., Tian, M. & Zhang, Y. Field-driven evolution of chiral spin textures in a thin helimagnet nanodisk. *Phys. Rev. B* **87**, 014401 (2013).

[32] Guslienko, K. Y. Skyrmion state stability in magnetic nanodots with perpendicular anisotropy. *IEEE Magn. Lett.* **6**, 1–4 (2015).

[33] Buda, L. D., Prejbeanu, I. L., Demand, M., Ebels, U. & Punadjela, K. Vortex states stability in circular Co(0001) dots. *IEEE Trans. Magn.* **37**, 2061–2063 (2001).

[34] Moutafis, C. *et al.* Magnetic bubbles in FePt nanodots with perpendicular anisotropy. *Phys. Rev. B* **76**, 104426 (2007).

[35] Moutafis, C., Komineas, S., Vaz, C. A. F., Bland, J. A. C. & Eames, P. Vortices in ferromagnetic elements with perpendicular anisotropy. *Phys. Rev. B* **74**, 214406 (2006).

[36] Gilbert, T. L. A phenomenological theory of damping in ferromagnetic materials. *IEEE Trans. Magn.* **40**, 3443–3449 (2004).

[37] Feldtkeller, E. Mikromagnetisch stetige und unstetige Magnetisierungskonfigurationen. *Z. Angew. Phys.* **19**, 530–536 (1965).

[38] Döring, W. Point singularities in micromagnetism. *J. Appl. Phys.* **39**, 1006–1007 (1968).

[39] Andreas, C., Kákay, A. & Hertel, R. Multiscale and multimodel simulation of Bloch-point dynamics. *Phys. Rev. B* **89**, 134403 (2014).

[40] Slonczewski, J. C. Properties of Bloch points in bubble domains. In *AIP Conf. Proc.*, vol. 24, 613–614 (1975).

[41] Thiaville, A., García, J., Dittrich, R., Miltat, J. & Schrefl, T. Micromagnetic study of Bloch-point-mediated vortex core reversal. *Phys. Rev. B* **67**, 094410 (2003).

[42] Lebech, B., Bernhard, J. & Freltoft, T. Magnetic structures of cubic FeGe studied by small-angle neutron scattering. *J. Phys.: Condens. Matter* **1**, 6105-6122 (1989).

[43] Wilhelm, H. *et al.* Confinement of chiral magnetic modulations in the precursor region of FeGe. *J. Phys.: Condens. Matter* **24**, 294204 (2012).

[44] Huang, S. X. & Chien, C. L. Extended skyrmion phase in epitaxial FeGe(111) thin films. *Phys. Rev. Lett.* **108**, 267201 (2012).

[45] Bak, P. & Jensen, M. H. Theory of helical magnetic structures and phase transitions in MnSi and FeGe. *J. Phys. C: Solid St. Phys.* **13**, L881-L885 (1980).

[46] Fischbacher, T., Franchin, M., Bordignon, G. & Fangohr, H. A systematic approach to multiphysics extensions of finite-element-based micromagnetic simulations: Nmag. In *IEEE Trans. Magn.*, vol. 43, 2896–2898 (2007).

[47] Fangohr, H. *et al.* Nmag - Computational Micromagnetics. URL `http://nmag.soton.ac.uk` (2012). Date of access 08/09/2015.

[48] Logg, A., Mardal, K. A. & Wells, G. N. *Automated solution of differential equations by the finite element method*, vol. 84 of *Lecture Notes in Computational Science and Engineering* (Springer Berlin Heidelberg, Berlin, Heidelberg, 2012).

[49] Pérez, F. & Granger, B. E. IPython: A system for interactive scientific computing. *Comput. Sci. Eng.* **9**, 21–29 (2007).

[50] IPython development team. IPython interactive computing. URL `http://ipython.org` (2015). Date of access 08/09/2015.

[51] Hunter, J. D. Matplotlib: A 2D graphics environment. *Comput. Sci. Eng.* **9**, 99–104 (2007).

[52] Hunter, J. D., Dale, D., Firing, E., Droettboom, M. & matplotlib development team. Matplotlib: python plotting - Matplolib 1.4.3 documentation. URL `http://matplotlib.org` (2015). Date of access 08/09/2015.

[53] Pauling, L. & Soldate, A. M. The nature of the bonds in the iron silicide, FeSi, and related crystals. *Acta Cryst.* **1**, 212 (1948).

[54] Richardson, M. The partial equilibrium diagram of the

Fe-Ge system in the range 40-72 at. % Ge, and the crystallisation of some iron germanides by chemical transport reactions. *Acta Chem. Scand.* **21**, 2305–2317 (1967).

[55] Yamada, H. Electronic structure and magnetism of FeGe with B20-type structure. *Phys. B Condens. Matter* **329-333**, 1131–1133 (2003).

[56] Grigoriev, S. V. *et al.* Critical fluctuations in MnSi near Tc: A polarized neutron scattering study. *Phys. Rev. B* **72**, 134420 (2005).

[57] Hamrle, J. *et al.* Determination of exchange constants of Heusler compounds by Brillouin light scattering spectroscopy: application to Co2 MnSi. *J. Phys. D. Appl. Phys.* **42**, 084005 (2009).

[58] Braun, H. B. Topological effects in nanomagnetism: from superparamagnetism to chiral quantum solitons. *Adv. Phys.* **61**, 1–116 (2012).

[59] Schulz, T. *et al.* Emergent electrodynamics of skyrmions in a chiral magnet. *Nat. Phys.* **8**, 301–304 (2012).

[60] Lee, M., Kang, W., Onose, Y., Tokura, Y. & Ong, N. Unusual Hall effect anomaly in MnSi under pressure. *Phys. Rev. Lett.* **102**, 186601 (2009).

AUTHOR CONTRIBUTIONS

M.B. and H.F conceived the study, and M.B. performed micromagnetic simulations. R.L.S. devised the analytic model and discussed its implications. R.C. contributed to the simulations and analysis of equilibrium states. D.C., M.-A.B., M.A., W.W., M.B., R.C., M.V., D.C.-O. and H.F. developed the micromagnetic finite element based simulator. M.V. and M.A. enabled running simulations on IRIDIS High Performance Computing Facility. M.B., H.F., R.L.S., and O.H. interpreted the data and prepared the manuscript.

COMPETING FINANCIAL INTERESTS

The authors declare no competing financial interests.

Supplementary Information: Ground state search, hysteretic behaviour, and reversal mechanism of skyrmionic textures in helimagnetic nanostructures

Marijan Beg,[1, *] Rebecca Carey,[1] Weiwei Wang,[1] David Cortés-Ortuño,[1] Mark Vousden,[1] Marc-Antonio Bisotti,[1] Maximilian Albert,[1] Dmitri Chernyshenko,[1] Ondrej Hovorka,[1] Robert L. Stamps,[2] and Hans Fangohr[1, †]

[1]*Faculty of Engineering and the Environment, University of Southampton, Southampton SO17 1BJ, United Kingdom*
[2]*SUPA School of Physics and Astronomy, University of Glasgow, Glasgow G12 8QQ, United Kingdom*

SUPPLEMENTARY SECTION S1: INITIAL MAGNETISATION CONFIGURATIONS

The magnetisation configurations that we use as initial states for the full three-dimensional micromagnetic simulations are shown in Supplementary Fig. 1. For every point in the d–H parameter space, we relax twelve different initial magnetisation configurations. These are the five skyrmionic configurations (A, B, C, D, and E), three helical configurations (H2, H3, and H4), the uniform configuration (U), and three random magnetisation configurations (R).

Now, we introduce an approximate analytic model that helps us generate a range of physically meaningful and reproducible initial skyrmionic magnetisation configurations labelled A-E in Supplementary Fig. 1. The used DMI energy density term (see Methods section of the main text) is consistent with the helimagnetic material of crystallographic class T, and one expects a skyrmionic texture configuration with no radial spin component (chiral skyrmion) to emerge [1]. Consequently, if we consider a two-dimensional disk sample of radius R in the plane containing the x and y axes, as shown in Supplementary Fig. 2 (b) inset, an approximation of the chiral skyrmionic magnetisation texture (for $D > 0$), in cylindrical coordinates (ρ, φ, z), is

$$
\begin{aligned}
m_\rho &= 0, \\
m_\varphi &= \sin(k\rho), \\
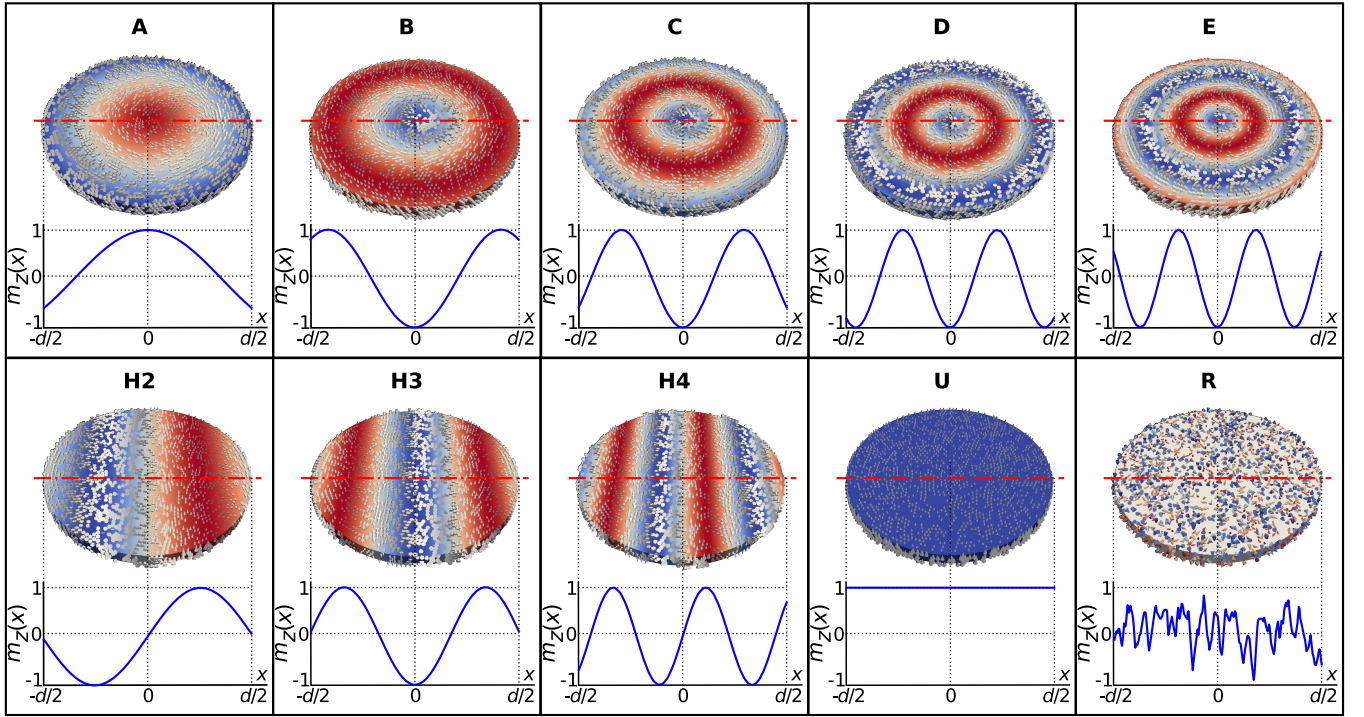m_z &= -\cos(k\rho),
\end{aligned}
\tag{1}
$$

FIG. 1. **The magnetisation configurations relaxed using the full three-dimensional micromagnetic simulations.** The configurations labelled A-E correspond to the first five solutions of the approximate analytic model, whereas the three helical states with 2, 3, and 4 helical half-periods are labelled as H2, H3, and H4, respectively. The uniform out-of-plane magnetisation state is labelled as U, and an example of random magnetisation state is marked with R.

where $k = 2\pi/s$ is a measure of the skyrmionic texture size s.

An equilibrium configuration requires that the torque exerted on the magnetisation $\mathbf{m}$ vanishes at every point in sample ($\mathbf{m} \times \mathbf{H}_{\text{eff}} = 0$), including the boundary. The effective field functional $\mathbf{H}_{\text{eff}} = -(\delta w/\delta \mathbf{m})/(\mu_0 M_{\text{s}})$, due to only symmetric exchange and DMI energy contributions, in absence of an external magnetic field is

$$\mathbf{H}_{\text{eff}} = \frac{2}{\mu_0 M_{\text{s}}} \left[A\nabla^2 \mathbf{m} - D\left(\nabla \times \mathbf{m} \right) \right], \tag{2}$$

for any magnetisation texture. Computing this expression for the radially symmetric approximate skyrmionic texture model $\mathbf{m} = \sin(k\rho)\hat{\boldsymbol{\varphi}} - \cos(k\rho)\hat{\mathbf{z}}$ results in

$$\begin{aligned}
\mathbf{H}_{\text{eff}} = & \frac{2}{\mu_0 M_{\text{s}}} \left[\left(Dk - Ak^2 - \frac{A}{\rho^2} \right) \sin(k\rho) + \frac{Ak}{\rho} \cos(k\rho) \right] \hat{\boldsymbol{\varphi}} + \\
& \frac{2}{\mu_0 M_{\text{s}}} \left[\left(\frac{Ak}{\rho} - \frac{D}{\rho} \right) \sin(k\rho) + \left(Ak^2 - Dk \right) \cos(k\rho) \right] \hat{\mathbf{z}}.
\end{aligned} \tag{3}$$

Consequently, the torque exerted on the magnetisation $\mathbf{m}$ is

$$\mathbf{m} \times \mathbf{H}_{\text{eff}} = \frac{2}{\mu_0 M_{\text{s}}} \left[\frac{Ak}{\rho} - \frac{D}{\rho} \sin^2(k\rho) - \frac{A}{2\rho^2} \sin(2k\rho) \right] \hat{\mathbf{r}}. \tag{4}$$

Requiring the torque to vanish at the disk boundary $\rho = R$ results in the zero-torque condition:

$$g(kR) \equiv -P\sin^2(kR) - \frac{\sin(2kR)}{2kR} + 1 = 0, \tag{5}$$

where $P = D/kA$. The analysis of this condition shows that the parameter P must satisfy the inequality $P > 2/3$ in order for $g(kR)$ to have roots and, thus, a skyrmionic texture core to exist in at least metastable equilibrium. In Supplementary Fig. 2 (a), we plot the zero-torque condition as a function of kR for different values of P. Since $P = 2/3$ is the boundary case (dotted line in the plot), all plots for $P < 2/3$ have no solutions, whereas the zero-torque condition has multiple solutions if $P > 2/3$.

The skyrmionic magnetisation configurations used as initial states in the energy minimisation process, corresponding to the zero-torque condition solutions (marked A-F) for $P = 2$, we show in Fig. 2 (c). In order to support the discussion of these magnetisation configurations, we compute the skyrmion number S, which for our approximate analytic model results in $S = (\cos(kR) - 1)/2$. Its dependence on kR, presented in Fig. 2 (b) as a dashed line, shows that the skyrmion number for the skyrmionic textures in confined nanostructures is not an injective function since it does not preserve distinctness (one-to-one mapping between kR and skyrmion number value S). Therefore, a different scalar value S_{a} is computed and from its dependence on kR, shown in Fig. 2 (b) as a solid line, we conclude that this scalar value is injective and provides necessary distinctness between S_{a} values for different skyrmionic states. The details about skyrmion number S and scalar value S_{a} are in the Methods section of the main text.

For the helical state, which emerges as a consequence of the Dzyaloshinskii-Moriya interaction considered in this work, we expect that the magnetisation vector at any point is perpendicular to the helical propagation direction (Bloch-wall-like configuration). Consequently, if both x and y axis are in the plane of the thin-film sample and the x axis is chosen as a propagation direction, the helical magnetisation configuration in Cartesian coordinates is

$$\begin{aligned}
m_x &= 0, \\
m_y &= \cos(k_{\text{h}}x), \\
m_z &= \sin(k_{\text{h}}x),
\end{aligned} \tag{6}$$

where $k_{\text{h}} = 2\pi/\lambda$, with λ being the helical period [2].

Now, we investigate whether the helical period λ in confined nanostructures is independent on the sample diameter, and if not, what are the helical period values that can occur in our simulated system. After relaxing helical configurations and varying both the helical period and disk sample diameter (up to 180 nm), we find that all relax to a limited set of helical states with different helical periods. More precisely, the observed relaxed helical states consist of either 2, 3, or 4 helical half-periods along the disk sample diameter, including the characteristic magnetisation tilting at the boundary [3]. Thus, we define three different helical magnetisation configurations as initial states with helical periods $2d/2$, $2d/3$, or $2d/4$, where d is the disk sample diameter, and are named H2, H3, and H4, respectively. Magnetisation configurations of these states, together with their $m_z(x)$ profiles along the horizontal symmetry, are shown in Supplementary Fig. 1.
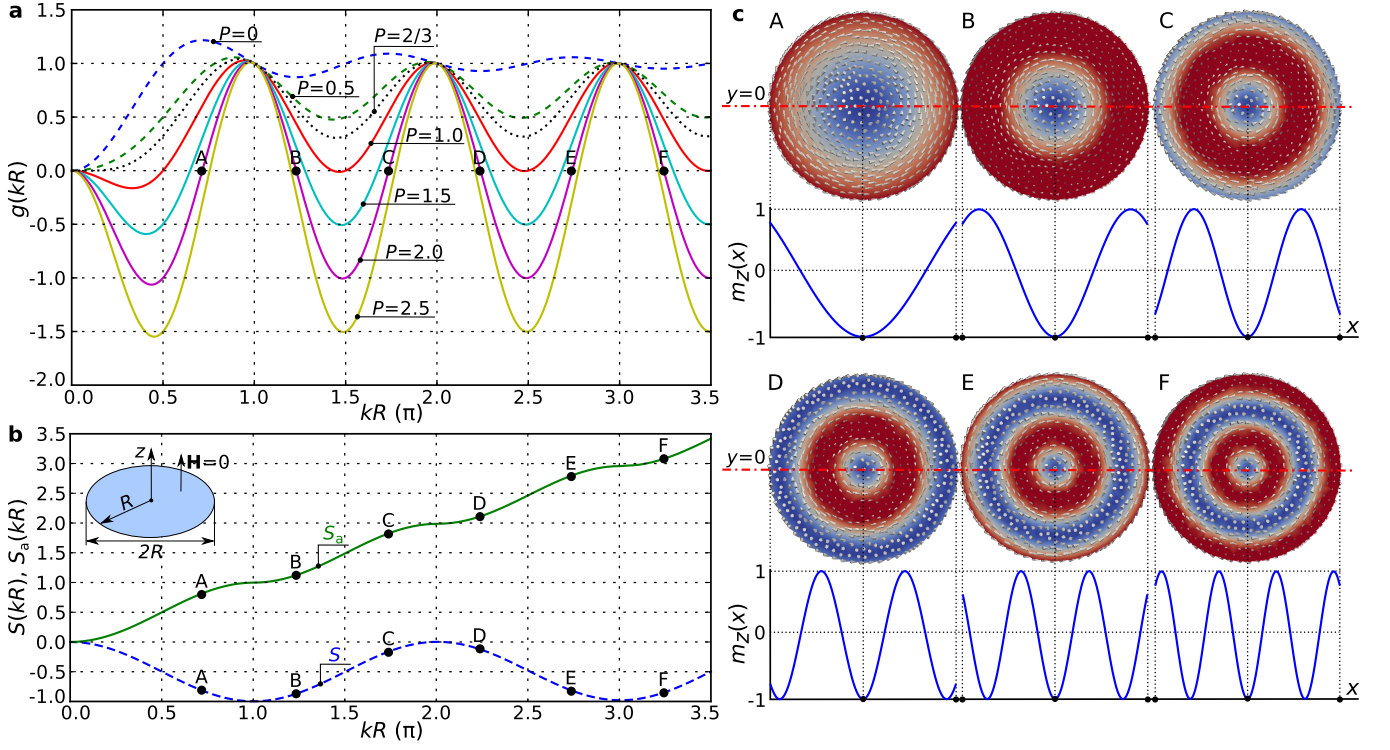
FIG. 2. **Zero-torque condition plots and magnetisation configurations corresponding to its solutions.** (**a**) The zero-torque condition $g(kR)$ plots, given by Eq. (5), for different values of $P = D/kA$. All zero-torque conditions for P smaller than the boundary case $P = 2/3$ (dotted line) have no solutions, whereas for $P > 2/3$, multiple solutions (A-F) exist. (**b**) The non-injective dependence of skyrmion number S and the injective dependence of scalar value S_a on kR. (**c**) The magnetisation configurations and the out-of-plane magnetisation component $m_z(x)$ along the horizontal symmetry line for different solutions (A-F) of Eq. (5) for $P = 2$.

In addition to the previously defined eight chiral initial states, we also use the uniform magnetisation configuration, where the magnetisation at all mesh nodes is in the positive out-of-plane z-direction, as shown in Supplementary Fig. 1 marked as U. Finally, in order to capture other equilibrium states that cannot be obtained by relaxing previously described well-defined magnetisation configurations, we also use additional three random magnetisation configurations. At every mesh node, we choose three random numbers in the $[-1, 1]$ range for three magnetisation components and then normalise them in order to fulfil the $|\mathbf{m}| = 1$ condition. An example of one random magnetisation configuration is shown in Supplementary Fig. 1 and labelled as R.

SUPPLEMENTARY SECTION S2: RELAXATION DIAGRAMS

In this section, we compute the equilibrium states at all points in the d–H parameter space obtained by relaxing well-defined initial states, introduced in the Supplementary Section S1. More precisely, we compute the equilibrium states (local energy minima) that result from a particular initial condition. This allows us to provide a systematic overview of equilibrium states, and gain additional insight about the phase space energy landscape in the studied system. We vary the sample diameter between 40 nm and 180 nm in steps of $\Delta d = 4$ nm and the external magnetic field between $\mu_0 H = 0$ T and $\mu_0 H = 1.2$ T in steps of $\mu_0 \Delta H = 20$ mT. Relaxation diagrams are represented by plotting the scalar value S_a as a function of disk diameter d and applied field strength H, and Supplementary Fig. 3 shows the relaxation diagrams for skyrmionic initial configurations A-E, and Supplementary Fig. 4 shows the relaxation diagrams for helical H2, H3, H4, and uniform U initial configurations. The phase diagram of equilibrium states, shown in Fig. 1 in the main text, summarises the main results from the relaxation diagrams presented and discussed here.

We now discuss each of relaxation diagrams in Supplementary Fig. 3 and 4, where each subplot corresponds to one particular initial configuration. The scalar value S_a, as a function of disk sample diameter d and external magnetic field
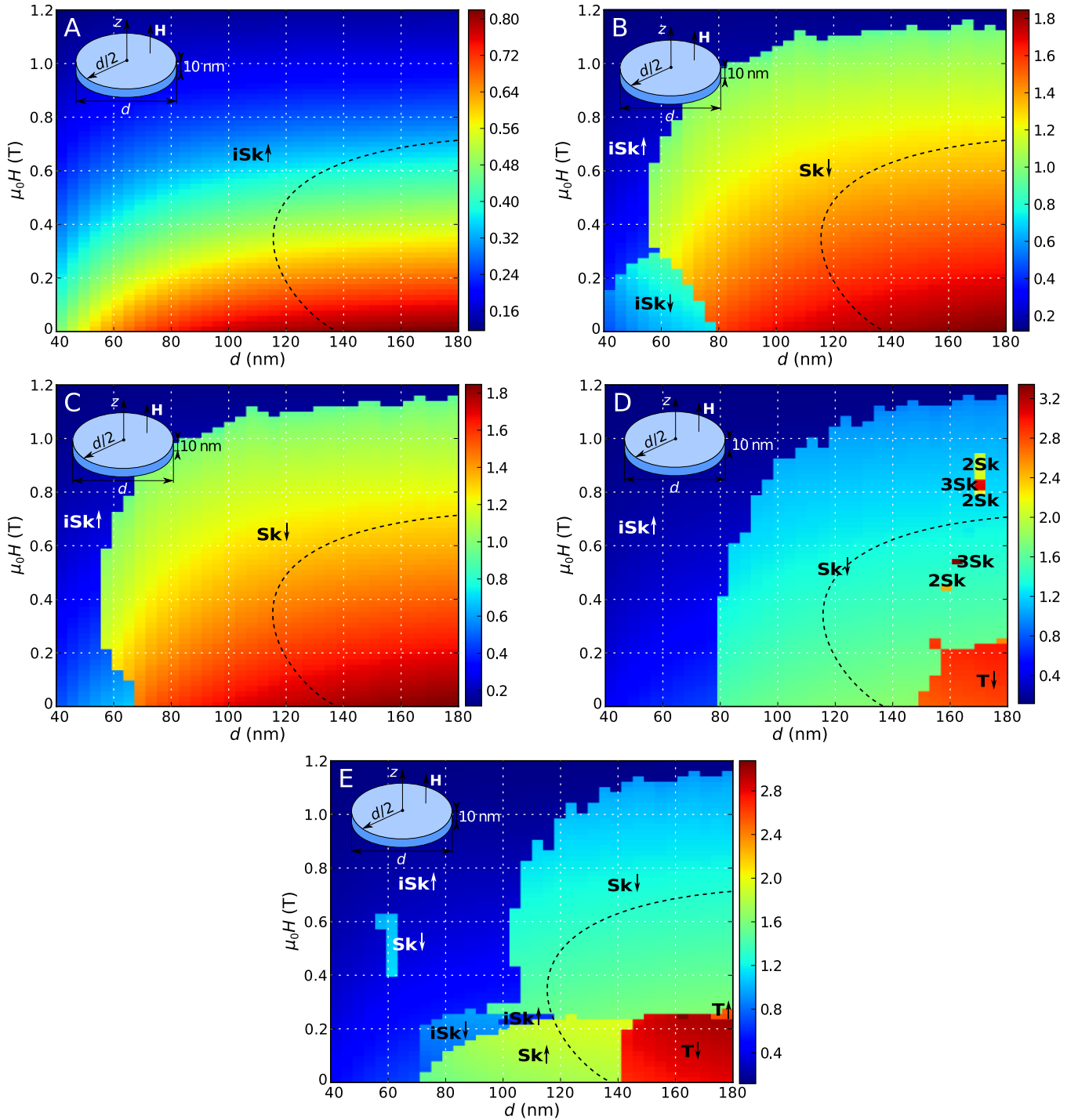
FIG. 3. **The relaxation diagrams obtained by relaxing skyrmionic initial state A-E.** The initial states correspond to the first five solutions of the analytic model and the phase diagrams are marked A-E accordingly. The relaxation diagrams are represented as the dependence of scalar value S_a on the disk sample diameter d and an external field H (as shown in insets).

H, computed for the final relaxed equilibrium state, i.e. local or global energy minimum, we show in Supplementary Fig. 3 (A) for the energy minimisation process that started from the skyrmionic initial configuration A (shown in Supplementary Fig. 1). The "iSk↑" label refers to the incomplete Skyrmion (iSk) magnetisation configuration with the core magnetisation pointing in the positive z-direction. An example of this state, marked with the same label, is shown in Supplementary Fig. 5. From the Supplementary Fig. 3 (A), we can see that for all examined diameters and external field values, the final relaxed configuration is the iSk↑ state. Now, this relaxation diagram is compared with
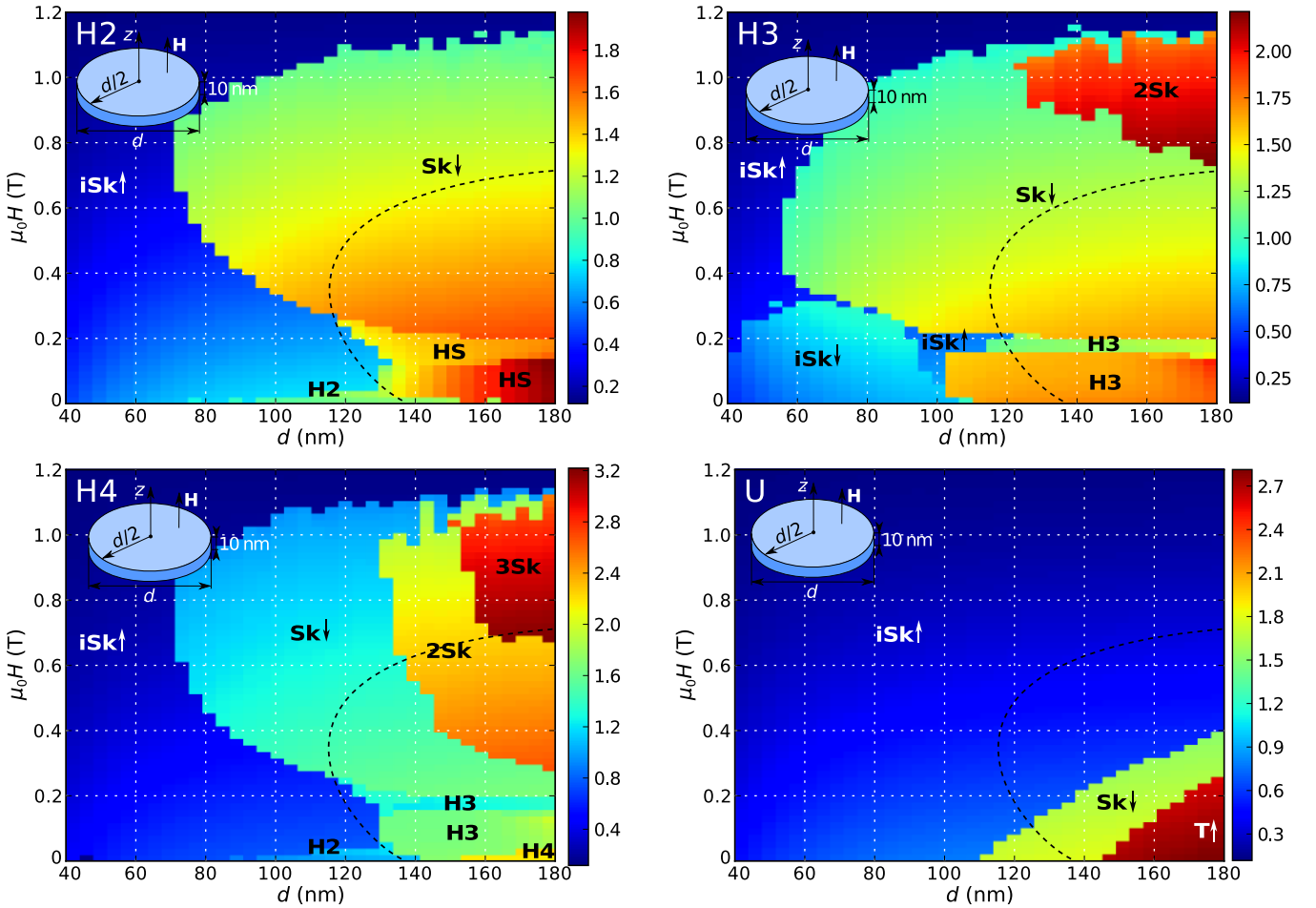
FIG. 4. **The relaxation diagrams obtained by relaxing helical and uniform initial state.** The initial states correspond to the helical states H2, H3, and H4, as well as the uniform state U, and the relaxation diagrams are marked accordingly. The relaxation diagrams are represented as the dependence of scalar value S_a on the disk sample diameter d and an external field H (as shown in insets).

the ground state phase diagram (see Fig. 2 (a) in the main text) and the boundary between two ground state (iSk and Sk) regions is shown as the dashed line in the discussed relaxation diagram. We can see that the iSk is indeed the ground state (i.e. the global energy minimum) for $d < 140\,\mathrm{nm}$, but for larger diameters the isolated Skyrmion (Sk) configuration has a lower energy, and thus the iSk configuration is only a local energy minimum.

Similarly, if the energy minimisation process is started from the initial configuration B, shown in Supplementary Fig. 1 (B), the $S_a(d, H)$ for the final relaxed magnetisation state is obtained and shown in Supplementary Fig. 3 (B). The vast majority of the final configurations ($d \geq 80\,\mathrm{nm}$ and $\mu_0 H \lesssim 1.1\,\mathrm{T}$), labelled as "Sk↓", correspond to the isolated skyrmion state with the core pointing in the negative z-direction. An example of this state we show in Supplementary Fig. 5, marked with the same label. By comparison with the ground state phase diagram shown in Fig. 2 (a) in the main text (dashed line), we can see that the Sk is the ground state for large diameters $d \geq 140\,\mathrm{nm}$ and field values $\mu_0 H < 0.7\,\mathrm{T}$. However, for smaller diameters the isolated skyrmion configuration is only metastable (as the iSk configuration is the ground state). We can see that in the vicinity of $d \approx 60\,\mathrm{nm}$ and $\mu_0 H \approx 0.1\,\mathrm{T}$ parameter space point, the initial configuration B relaxes to the incomplete skyrmion state with core oriented in the negative z-direction (iSk↓), but for larger field values, configuration B falls into the iSk↑ configuration (see Supplementary Fig. 5 for detailed configurations of iSk↓ and iSk↑ states). The iSk↓ has a higher energy than the iSk↑ as the majority of the magnetisation is pointing in the direction opposite to the applied field. However, the initial configuration B is such that the core is pointing down, and there appears to be a direct energy minimisation path to the iSk↓ configuration for field values smaller than approximately $0.3\,\mathrm{T}$. For larger fields, the Zeeman energy becomes so important that the initial configuration B leads to the the iSk↑ configuration.

Supplementary Fig. 3 (C) shows that the initial configuration C suppresses the iSk↓ state completely but is otherwise
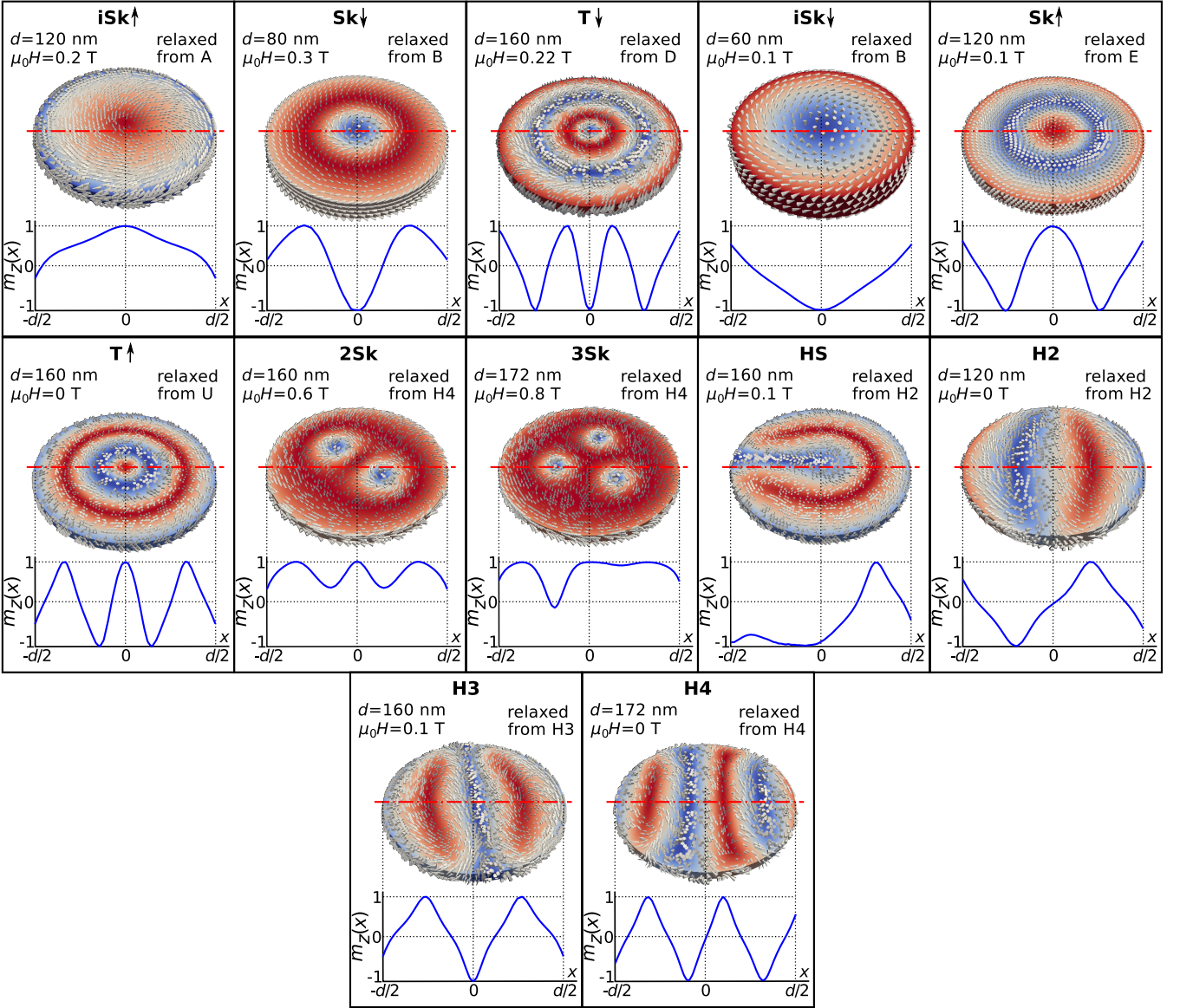
FIG. 5. **The identified equilibrium magnetisation configurations.**

similar to Supplementary Fig. 3 (B). We note in particular that the Sk configuration cannot exist for $d < 60\,\text{nm}$ even if the relaxation is started from a Sk-like configuration B or C, i.e. there are no metastable isolated skyrmion states at the smallest diameters.

If the system is relaxed from the initial state D, shown in Supplementary Fig. 1 (D), a qualitative change from Supplementary Fig. 3 (B) and (C) is evident as shown in Supplementary Fig. 3 (D). In addition to the iSk↑ and Sk↓ states, there are now a number of, according to Fig. 3 in the main text, higher energy metastable states emerging as 2 or 3 skyrmions in the disk (see Supplementary Fig. 5 for detailed plots of 2Sk and 3Sk states). Furthermore, for small field values $\mu_0 H \lesssim 0.2\,\text{T}$ and large diameters $d \gtrsim 152\,\text{nm}$, the Target (T) equilibrium state with core orientation in the negative z-direction (T↓) arises. The T↓ state is shown in Supplementary Fig. 5.

The scalar value $S_a(d, H)$ computed for final equilibrium configurations in Supplementary Fig. 3 (E) we obtained by relaxing the initial configuration E shown in Supplementary Fig. 1. The initial skyrmionic state E does not relax to 2 and 3 skyrmion configurations but allows the Sk↑ state to arise for small field values.

Supplementary Fig. 4 (H2), (H3) and (H4), show the $S_a(d, H)$ for starting configurations H2, H3 and H4, respectively, as shown in Supplementary Fig. 1. All three initial configurations result in the incomplete Skyrmion configuration with core pointing up (iSk↑) for the smallest diameters as well as for largest fields. The H3 initial
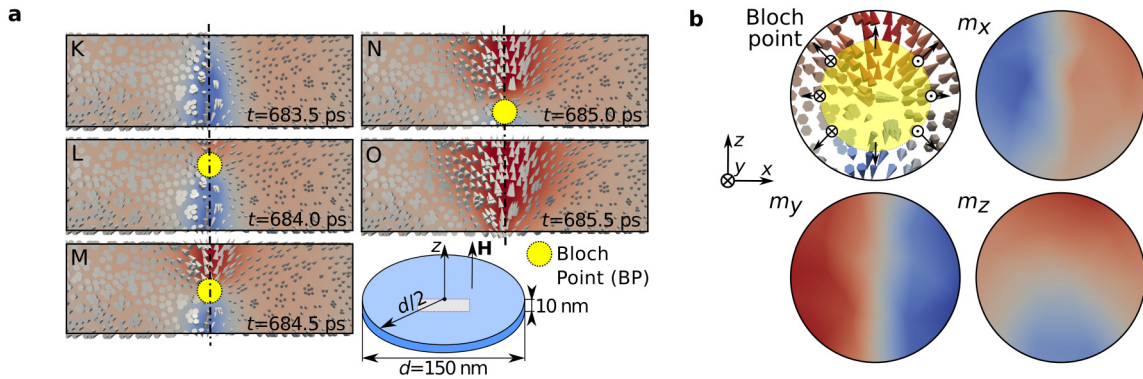
FIG. 6. **The isolated skyrmion orientation reversal in confined three-dimensional helimagnetic nanostructure with downwards Bloch point propagation direction.** (**a**) The m_z colourmap and magnetisation field in the central part of xz cross section as shown in an inset together with the position of Bloch Point (BP). (**b**) The BP structure along with colourmaps of magnetisation components which shows that the magnetisation covers the closed surface (sphere surrounding the BP) exactly once.

configuration relaxes into a configuration with two Skyrmions in the disk (2Sk) for $d > 120$ nm and field values between 0.8 T and 1.1 T. These 2Sk configurations had appeared occasionally when starting from configuration D (see Supplementary Fig. 3 (D)). The H4 initial configuration also encourages 3 skyrmions in the disk to arise as a metastable state.

Supplementary Fig. 5 (U) shows S_a for final configurations when the simulation starts from a uniform magnetisation, pointing up in the positive z-direction. This results mostly in the incomplete Skyrmion configuration with core pointing up (iSk↑). However, we also find the Skyrmion with core pointing down Sk↓ and the Target configuration T↑ as the diameter increases and the field decreases. Supplementary Fig. 3 (A) is interesting to compare with Supplementary Fig. 4 (U): in the former, only the iSk↑ state results, presumably because from the initial state A, only the iSk↑ state is accessible in the relaxation. On the contrary, for the uniform configuration, the system finds the energy minimum for the isolated Skyrmion state Sk↓ and the Target T↑ because other energy minima can be accessed from this initial state. Fig. 5 (a) in the main text shows the relative energies of the different metastable states for $H = 0$.

SUPPLEMENTARY SECTION S3: DIFFERENT BLOCH POINT PROPAGATION DIRECTION

In order to illustrate a different direction of the Bloch Point (BP) propagation, we show a result from another skyrmion reversal. The simulation parameters are the same as in Fig. 7 of the main text, except that the Gilbert damping α is increased from 0.3 to 0.35. We show the results of isolated skyrmion core orientation reversal dynamics with modified Gilbert damping in Supplementary Fig. 6.

Now, the obtained reversal dynamics is compared with the reversal dynamics shown in Fig. 7 in the main text. From the Supplementary Fig. 6 (a), we can see that the Bloch point enters the sample at the top boundary at approximatelly 684 ps, then propagates downwards to the bottom boundary, where it leaves the sample at approximatelly 685 ps. Because of the opposite BP propagation direction, the structure of the Bloch Point changes (compare Fig. 7 (e) in the main text with Supplementary Fig. 6 (b)). More precisely, the out-of-plane magnetisation component m_z field in the vicinity of BP is changed so that for the upper half of BP $m_z > 0$, whereas in the lower half $m_z < 0$.

SUPPLEMENTARY SECTION S4: HIGHER ORDERING TEMPERATURE MATERIAL

The ordering temperature of simulated FeGe material, $T_C = 278.7$ K [4], is lower than the room temperature, which means that this material cannot be used to fabricate a device operating at room temperature. Therefore, it is important to determine how our results regarding the identified lowest energy state would change for the material with higher ordering temperature. Because no high ordering temperature helical B20 material has been reported to this day, the best we can do is to artificially increase the ordering temperature, estimate new material parameters, and repeat the study of equilibrium states.
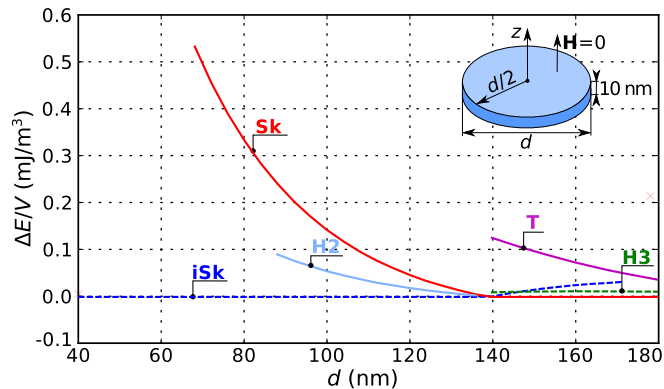
FIG. 7. **The energy density differences between all identified equilibrium states and corresponding lowest energy state as a function of disk sample diameter.** A full set of initial state configurations are relaxed for different disk sample diameter values at zero external magnetic field. The helimagnetic material ordering temperature is artificially increased to $T_C = 350 \, \text{K}$ (above room temperature).

We increase the ordering temperature to $T_C = 350 \, \text{K}$, and calculate new values of exchange and Dzyaloshinskii-Moriya energy constants (following the estimation described in Methods section of the main text) and obtain $A = 1.1 \times 10^{-11} \, \text{J/m}$ and $D = 1.98 \times 10^{-3} \, \text{J/m}^2$. Using these values, we relax the full set of initial magnetisation configurations at zero external magnetic field for different disk sample diameters. More precisely, we vary the disk sample diameter between $40 \, \text{nm}$ and $180 \, \text{nm}$ in steps of $4 \, \text{nm}$ and compute the energy density E/V of all identified relaxed equilibrium states, where V is the sample volume. After that, from the computed energy density, we subtract the energy density of the corresponding lowest energy state. We plot the calculated energy density differences of all equilibrium states as a function of disk sample diameter d and show them in Supplementary Fig. 7.

By comparing the Supplementary Fig. 7 for higher ordering temperature material with Fig. 3 in the main text, we conclude that the incomplete Skyrmion (iSk) state remains being the lowest energy state for $d < 140 \, \text{nm}$, whereas the isolated Skyrmion (Sk) state is the lowest energy state for $d \geq 140 \, \text{nm}$. However, the iSk state is not in equilibrium for disk sample diameters larger than $172 \, \text{nm}$, which is in contrast to the FeGe material case where iSk is in equilibrium for all examined d values. Another difference is that the metastable Target (T) state is the highest energy state for the whole d range where it is in equilibrium. Finally, we do not observe H4 state (helical state with four half periods) for this high ordering temperature material.

SUPPLEMENTARY REFERENCES

---

* mb4e10@soton.ac.uk

† h.fangohr@soton.ac.uk

[1] Rößler, U. K., Bogdanov, A. N. & Pfleiderer, C. Spontaneous skyrmion ground states in magnetic metals. *Nature* **442**, 797–801 (2006).

[2] Bak, P. & Jensen, M. H. Theory of helical magnetic structures and phase transitions in MnSi and FeGe. *J. Phys. C: Solid St. Phys.* **13**, L881-L885 (1980).

[3] Rohart, S. & Thiaville, A. Skyrmion confinement in ultrathin film nanostructures in the presence of Dzyaloshinskii-Moriya interaction. *Phys. Rev. B* **88**, 184422 (2013).

[4] Lebech, B., Bernhard, J. & Freltoft, T. Magnetic structures of cubic FeGe studied by small-angle neutron scattering. *J. Phys.: Condens. Matter* **1**, 6105-6122 (1989).